Visualizing Three-Dimensional Variations in The Mineral Distribution of Black Smoker Chimneys

Master of Science Thesis

Solveig Adine Osjord

Department of Earth Science

University of Bergen

January 2023

Abstract

The last few decades have raised an increased interest in the research of hydrothermal deposits at the Arctic Mid Ocean Ridge (AMOR), both for scientific purposes and as a potential resource for critical minerals. However, resource estimates based on the extrapolation of the abundances of base-metal sulfide minerals are complicated by their heterogenous distribution in natural samples. To get a better understanding of the spatial distribution of minerals in hydrothermal deposits, Computed Tomography (CT) scanning is introduced as a tool. In this study, I try to incorporate CT-scanning for quantifying the amount of relative mineral proportions in hydrothermal chimneys based on grayscale imaging. The results show that CT-scanning is a good tool for spatially and non-destructively visualizing the abundance of different minerals. However, there are several limitations related to the method 1) minerals with high density produce noise and streaking artifacts to the images, and therefore reduce the quality of the scans, 2) the relatively coarse voxel resolution of CT-imaging limits the detection of minerals with small grain size, 3) separation of distinct mineral phases with relatively similar density remains challenging, 4) big samples create a lot of noise as photons are being detected several times and produce artifacts to the images. The study found that the most abundant minerals in the chimneys were possible to identify using the 3D-imaged data, however the type of minerals had to be determined using supplementary 2D analysis such as scanning electron microscopy (SEM), Raman spectroscopy and reflected light microscopy. By applying gaussian mixture modelling to the 3D-data for determining the mineral populations, scanning large chimneys multiple times to resolve the issue of samples being too large, and applying additional complementary imaging techniques and/or geochemical analysis to identify the unidentified minerals, the CT-scanning method might be further improved.

Acknowledgements

Bergen, January 2023
Solveig Adine Osjord

Table of contents

Glossary / abbreviations

AMOR – Arctic Mid Ocean Ridges

AVR – Axial Volcanic Ridge

BSE – Backscattered electrons

CT – Computed Tomography

EDS – Energy Dispersive X-ray Spectroscopy

REE – Rare earth elements

SEM – Scanning Electron Microscopy

SMS – Seafloor massive sulfide (deposit)

Streaking – Artifact on the CT-scans produced either by beam hardening and/or scattered photons.

VMS – Volcanic massive sulfide (deposit)

Voxel – equivalent of pixels, except that it is in 3D instead of 2D

1. Introduction

The demand for minerals and metals is growing rapidly in response to the ongoing energy transition to more renewable energy sources as a measure for reducing the emission of greenhouse gasses (Viebahn et al., 2015), which has accelerated the need for alternative minerals and metals. Necessary technologies for this transition range from solar power, electricity storage, wind power, hydrogen generation and storage, and ferrous alloys, which all demand what Viebahn et al. (2015) refer to as *critical minerals*. According to Viebahn et al. (2015), critical minerals are defined as minerals that are essential for modern industries and cannot be substituted, such as chalcopyrite and sphalerite. At present, these minerals are predominantly extracted from mineral deposits contained in the continental crust, such as volcanic-hosted massive sulfide (VMS) deposits on land (Hannington et al., 2011). This has raised an interest in discovering new sources of these minerals, which ultimately lead to this study. Critical metals in these minerals are for instance silver, nickel, potassium, lithium, cobalt, copper, and some rare earth elements (REE) (IEA, 2021).

Recent studies have focused especially on mineral deposits that can be found on the seafloor, such as polymetallic nodules, ferromanganese crusts and seafloor massive sulfides (SMS) (Murton et al., 2019). The latter is interpreted as the modern analog for volcanic-hosted massive sulfide deposits on land, and forms in high-temperature hydrothermal systems on spreading ridges, back-arcs and on submarine volcanic arcs (Hannington et al., 2005, German and Von Damm, 2006). Here, circulation of seawater below the seafloor results in dissolution of metals into hot and buoyant fluids, from which metal-rich sulfides precipitate below and above the seafloor when fluids rise up to the surface and cool down (Tivey, 2007). In their study from 2018, Lusty and Murton found that the resulting sub-seafloor mineral deposits, hydrothermal chimneys and metalliferous sediments may host substantial amounts of critical minerals (Lusty and Murton, 2018). The ability to accurately estimate the total resource potential of such seafloor massive sulfides has however proven to be challenging. For example, Hannington et al. (2011) argue that the total reserves of massive sulfides in the neovolcanic zones amount to $3 \cdot 10^7$ tons Cu + Zn, whereas Cathles (2011) estimate that the total metal resources on the entire seafloor totals at $530 \cdot 10^9$ tons, nearly 18 000 times

higher than the findings of Hannington et al. (2011). In addition, seafloor drilling at the Solwara 1 massive sulfide deposit highlights the importance of obtaining knowledge from subsurface mineralization in addition to sampling the more easily accessible hydrothermal chimneys on the seafloor, which can significantly differ in copper grade weight percentages (6.8% Cu versus 11%, respectively) (Ltd., 2012). Furthermore, hydrothermal chimneys may represent highly localized metal accumulations with concentrations that are not necessarily representative for the underlaying and surrounding oceanic crust – resulting in high grades but subeconomic tonnage (Ltd., 2012). Hence, chimney sampling may introduce a significant sampling bias. Thus, an improved understanding of the metal distribution in seafloor mineral deposits in three dimensions (3D) is essential for rigorously assessing their resource potential (Petersen et al., 2018). X-ray Computed Tomography (CT) potentially allows for the fast and non-destructive assessment of the distribution of metal sulfide minerals in 3D. Although initially mostly used for medical applications, the technique has gained increased attention in the solid Earth sciences over the last decade, even abord scientific drilling vessels (i.e. Chikyu (Taira et al., 2014)) to readily characterize rock cores recovered from the seafloor. Since CT imaging essentially measures a material's X-ray attenuation that is a function of its atomic weight (Z) (Hounsfield, 1972), atomically heavy sulfide minerals are expected to produce a distinctive contrast compared to for example atomically light silicate matrix. Hence, CT imaging has the potential to yield quick and accurate estimate of metal-sulfide mineral distributions in seafloor and subseafloor samples. In this study we will test the viability of the technique, under the hypothesis that 3D-imaging of chimney structures may produce more realistic estimations of the metal abundances in the deposits, by visualizing the spatial distribution of sulfide minerals in the samples.

1.1 Purpose of the study

In this study, we will conduct the first ever known test of the application of such computed tomography-imaging (CT) techniques to visualize 3D-structures and the distribution of sulfide minerals in hydrothermal chimneys. The research questions in this project are therefore formulated as follows:

- What are the methodological requirements and limitations for the CT-scanning of hydrothermal chimneys?

- To what extent can 3D mineralogical variations in hydrothermal chimneys be detected by CT-scanning?

- How does 3D imagery from CT-scanning compare to the more traditional 2D analysis such as optical or electron microscopy techniques?

- What advantages does CT-scanning provide over other imaging techniques, and can this method be used to improve our understanding of the hydrothermal mineral resources at the seafloor?

2. Theoretical Background

2.1 Hydrothermal Systems

Hydrothermal vents were first discovered at the Galapagos rift in 1977 (Corliss et al., 1979), and the discovery has led to an extensive increase in the exploration of the seafloor (Hannington et al., 2011). Hydrothermal systems are found to be particularly abundant in spreading ridge areas such as mid-ocean ridges compared to the other settings (Hannington et al., 2005), and most of the hydrothermal vent systems along the mid-ocean ridges are typically hosted in mid-ocean ridge basalt (Tivey, 2007). Seawater is one of the main contributors for hydrothermal systems, since seawater circulation is required for material transport and deposition (Tivey, 2007). For water to circulate in a hydrothermal system, there are a few criteria that must be fulfilled. Firstly, there must be a heat source such as a spreading center hosting volcanic activity. Secondly, the water needs to penetrate the bedrock below the seafloor through a permeable fracture network (Tivey, 2007). When faulting occurs and fractures are exposed at the seafloor, the ocean water will saturate the crust. As a result of heating, the water will start to circulate through the crust along flow paths connecting recharge and discharge zones (Tivey, 2007). During this journey, the seawater modifies the composition of the oceanic crust, the ocean chemistry and provide metal-rich hydrothermal deposits in areas where venting occurs (Tivey, 2007). After penetrating the seafloor and being exposed to a heat source, the fluids have undergone a great temperature increase before reaching the seafloor. When the fluids eventually escape the crust and reach the seafloor, they produce a warmer area at the seabed, that together with changed chemical energy, is often associated with biological and microbial life (Tivey, 2007). Fluids venting at hydrothermal discharge sites will quench when in contact with cold ocean bottom water and precipitate minerals that are soluble at high temperatures (Tivey, 1998, Tivey, 2007).

The effects of hydrothermal circulation on the bedrock composition, varies depending on the spreading rates of the diverging plates. The varying spreading rate of mid-ocean ridges is classified in 5 main categories: ultraslow, slow, intermediate, fast and ultrafast spreading rates (D. Knight et al., 2018). Thin oceanic crust is associated with fast spreading ridges. The combination of fast spreading and thin crust results in circulation cells that are quite shallow, around 1-2 km deep (Hannington et al., 2005). Both intermediate and slow spreading ridges

occur in extension regimes where the crust is thick. Both ensure that the seawater penetrates deeper in the system, as far as 5-8 km below the oceanic crust, and may therefore also transport metals from greater depths than faster spreading ridges (Hannington et al., 2005). Ultraslow spreading ridges form under conditions where the spreading rate is lower than 12 mm yr^{-1} (Dick et al., 2003). They consist of linked magmatic and amagmatic accretionary segments, have discontinuous volcanism and usually lack transform faults (Dick et al., 2003). When spreading rates drop below 20 mm per year, the produced crust is thinner as a result of decreased volcanic activity in the area (Pedersen et al., 2010a). The first high-temperature venting at ultra-slow spreading ridges was found during a research cruise along the Southwestern Indian Ridge (SWIR) in 1997 (German et al., 1998). The venting at the SWIR was found after a study by German et al. (1996) suggested that the extent of hydrothermal activity along (ultra-)slow spreading ridges was likely underestimated. The Arctic Mid-Ocean Ridges (AMOR) in the Norwegian-Greenland Sea for example, host ridges which represent some of the slowest spreading ridges on Earth (Pedersen et al., 2010a). These ridges are dominated by frequent fault activity (Soule, 2015).

2.2 Vent fluid chemistry

The vent fluid chemistry provides important insight into the alteration process controlling the bedrock chemical modification and mineral precipitation at seafloor hydrothermal vent sites (German and Von Damm, 2006). Pressure and temperature conditions during the journey of the hydrothermal fluids are reflected in the chemistry of the fluids that seep out at the seafloor (German and Seyfried, 2014). Consequently, this can yield information about the depth of the heat source, because the depth of the fluid circulation can be calculated (German and Seyfried, 2014). There are four main factors for hydrothermal circulations; phase separation, water rock-interactions, biological processes and magmatic degassing (German and Seyfried, 2014). Reactions between seawater and sediments/seabed rocks commence as soon as the water enters the recharge zone and is exposed to increasing pressure and temperature, although pressure and temperature in this part of the system are still low (German and Von Damm, 2006, Tivey, 2007). During water-rock interactions, chemical elements are both lost and gained from the fluid (German and Seyfried, 2014). When the seawater reaches the reaction zone/root zone near a magmatic heat source, the temperature

increase is significantly higher than in the recharge zone (Alt, 1995). The maximum temperature of these hydrothermal fluids can exceed 400°C (German and Seyfried, 2014). As a result of the high temperature, fluid buoyancy further increases resulting in a rapid rise from the heat source, through the discharge zone before discharge at the seafloor vent site (German and Von Damm, 2006, German and Seyfried, 2014). During this last part of the system, the fluids dissolve and/or precipitate sulfide phases as they move toward the surface (Tivey, 2007). At the seabed, mixing with cold seawater drives mineral precipitation as a result of decreased mineral solubility upon cooling (Tivey, 2007, Tivey, 1998). The type of minerals precipitated is related to the temperature of the hydrothermal fluid, as the solubility of elements such as copper, iron and zinc shows different temperature dependencies (Seyfried, 1987, Butterfield et al., 1994, John et al., 2008). A schematic illustration of the circulation is provided in Figure 2.1.
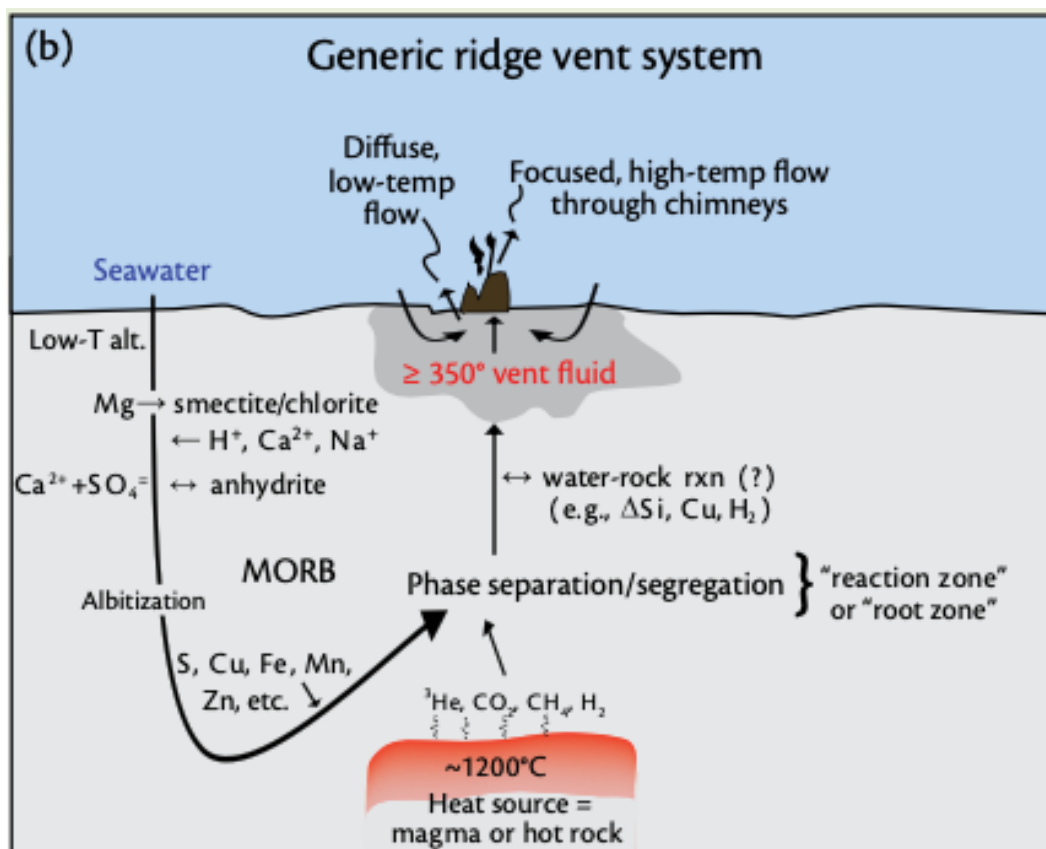
Figure 2.1: Schematic walkthrough of the hydrothermal circulation along mid ocean ridges. The seawater enters the seabed through fissures and fractures and enters the recharge zone where low temperature alterations are applied. Thereafter, the water moves further down until it reaches the heat source and the reaction/root zone where it undergoes phase separation. Lastly the buoyant hot fluid moves rapidly through the discharge zone and reaches the seafloor (Tivey, 2007). Figure from Tivey (2007).

2.3 Black smoker chimney growth

Hydrothermal chimneys are deposited when hydrothermal fluids react with seawater from the sea floor and rapid cooling occur (Haymon, 1983). Cooling of the hydrothermal fluid results in precipitation of minerals and the buildup of hydrothermal chimneys. In areas where hydrothermal fluids have lower temperatures and persistent outflow, microorganisms are known to take part in the mineral precipitation processes through biomineralization (Johannessen et al., 2017). The chimney growth model is often referred to as a two-stage model, with respectively a sulfate-dominated stage (1) and a sulfide replacement stage (2) (Figure 2.2) (Haymon, 1983). Once high temperature hydrothermal fluids vent on the seabed and react with the cold seawater, minerals start to precipitate. Precipitation of anhydrite happens because seawater contains Ca^{2+} and SO_4^{2-} ions that when heated to 150°C or more, combine and form anhydrite (Tivey, 1998). The anhydrite forms upwards and outwards around the vent, forming the initial chimney walls in the form of a ring (Haymon, 1983). The outer edge of the chimney is dominated by fine grained minerals such as sphalerite, pyrite and pyrrhotite. These sulfide minerals will consequentially be laminated in the walls of the chimney, as the anhydrite continues to grow outward (Haymon, 1983). When chimney walls are fully developed and contain mainly anhydrite, stage 1 is complete. Stage 2 is mainly dominated by sulfide precipitation. As fluids continue to flow through the center of the chimney, it reacts with the anhydrite, and precipitates sulfide minerals that replace the anhydrite. This process is mainly dominated by chalcopyrite precipitation on the inner wall of the chimney (Tivey, 1998). The further growth continues upwards by depositing more anhydrite, and inwards toward the conduit precipitating sulfides (Haymon, 1983).

STAGE I
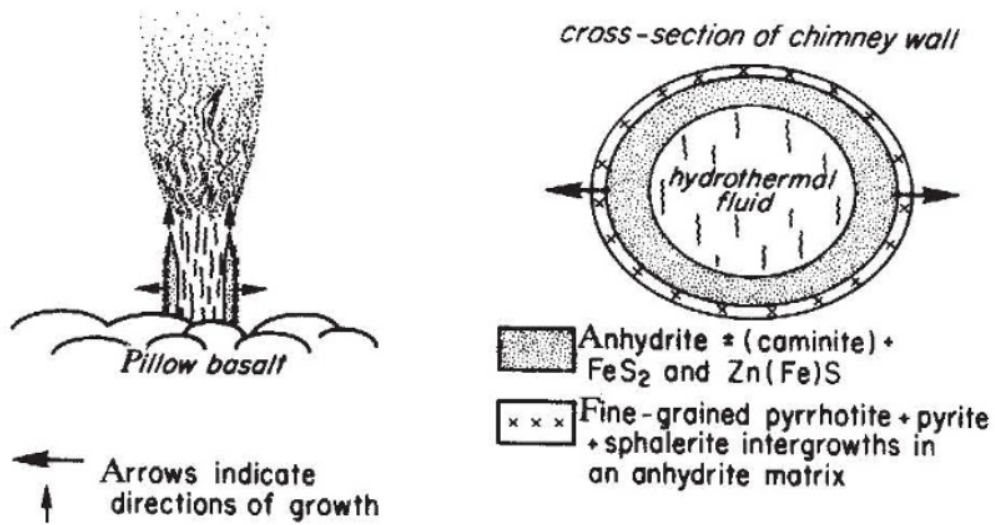
STAGE II
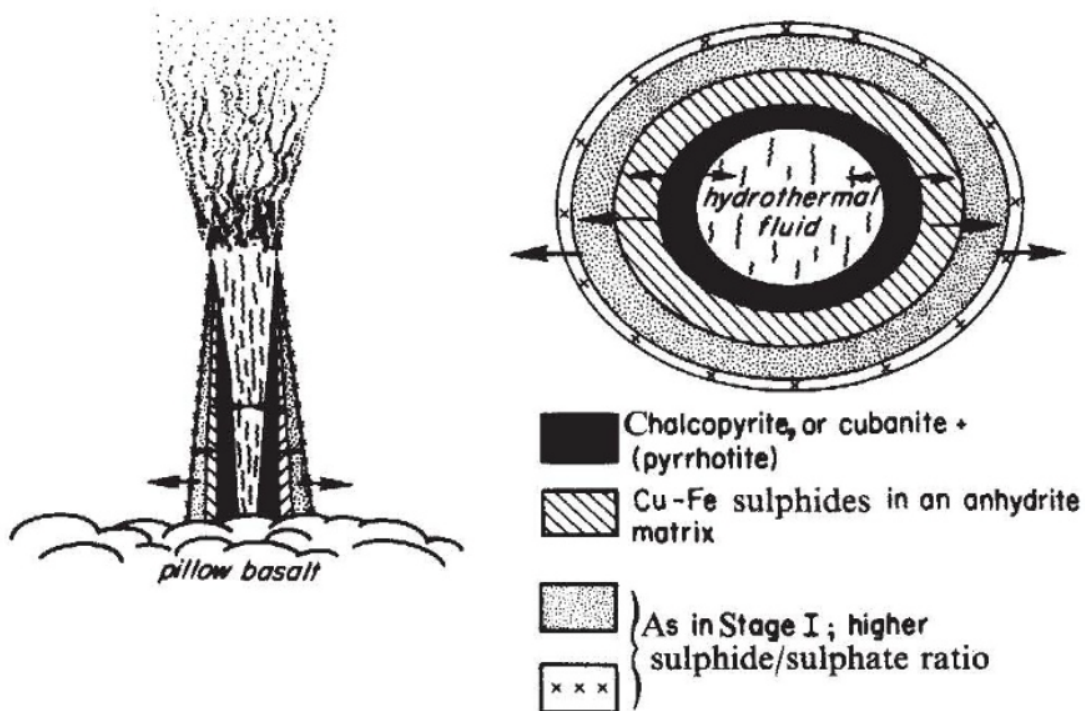
Figure 2.2: Visual representation of the two-stage growth model. 1) primary anhydrite is forming in a ring around the vent, creating the first walls of the chimney. Fine grained sulfide precipitants are forming on the outer edge of the anhydrite wall and will after continued precipitation of anhydrite soon be laminated in the anhydrite walls. 2) Mainly dominated by sulfide precipitation. Chalcopyrite is precipitated in the inner rim of the chimney walls, whereas additional sulfides (pyrite and sphalerite) are still precipitating on the outer rim of the chimney walls. Both sulfides on the inner and outer rim of the walls start to replace anhydrite as they precipitate (Haymon, 1983). Model from Haymon (1983).

2.4 Computed Tomography (CT)

Computed tomography (CT) is a scanning technique that obtains X-ray imagery from an object that can be visualized in 3-D, based on the density contrasts within the investigated sample. The first CT-scanner was developed by Godfrey Newbold Hounsfield in 1967 (Willems et al., 1979), which uses X-ray radiation directed at the object of choice from an external source to produce the imagery (Hounsfield, 1972). X-rays are directed at an object, where the amount of radiation attenuated determines what is detected by the detector. The original CT-scanners worked in this particular way; both the source and detector were orbiting around the object to ensure that X-rays were directed at the object from multiple directions. These orbits moved 360 degrees around the object and produce slices or 2D pictures of the density contrasts that can be reconstructed in 3D (Hounsfield, 1972). The first CT-scanners on the market operated with a single beam source and detector arrangement, whereas the more advanced CT-scanners in modern times use a fan-beam geometry where multiple X-rays are shot at the time, and the source rotates within a fixed ring of high-efficiency detectors (Wellington and Vinegar, 1987). The source is a tube that rotates around the object, whereas the signals are detected by either a stationary or moving detector (Hsieh, 2003). Depending on the purpose of scanning, the setup of the system can vary. For the purpose of this project, an industrial scanner is used rather than a medical scanner. The difference in this case is that the sample is spinning around its own axis, while the distance between the samples and the source/detector can be adjusted, however both the source and the detector have permanent positions during the scans. When working with 3D reconstructions, the degree of attenuation, and therefore also the density relationships, are visualized as distinct voxel grayscale values (Razi et al., 2014). Dark areas on the CT-scanned images reflect areas where the linear attenuation coefficient (LAC) is low, which indicate a substance of low density, whereas bright areas indicate high LAC values, and also high density substances (Wan et al., 2015). As technology has improved over the years, micro and nano CT-scanning has provided even higher spatial resolution than the original medical CT-scanners, making it possible to study substances at a cellular scale and nanometer scale (Peyrin et al., 2014). For example, trabecular bones can be imaged with voxel sizes between 5-20 micrometers with use of a micro-CT system and the nano-CT system SkyScan221 can give spatial resolution at 600 nanometers (Peyrin et al., 2014).

2.5 Computed Tomography (CT) in geosciences

CT-scanning has been used in geoscience for several decades. Already in 1982 CT-scanning was used to study bulk densities in soils by Petrovic et al. (1982). Thereafter in 1987, Vinegar and Wellington (1987) reported that CT-scanning was a useful tool in petroleum engineering to quantify density and porosity in rock samples. In 1989 CT-imagery was used to study structures and fabrics in sedimentary rocks (Renter, 1989). The application of CT-scanning in geosciences allows the use of a non-destructive technique that can visualize the internal structure of an object in 3D (Mees et al., 2003). The use of CT-scanning as a tool in geosciences still relevant and increasing. It is being used for the detection of invisible volcanic ash layers in sediment cores (van der Bilt et al., 2021), quantification of ice-rafter debris in sediment cores (Cederstrøm et al., 2021) and visualization of flow paths in a simulated hydrothermal chimney (Barge et al., 2020).

3. Geological setting

3.1 The Arctic Mid Ocean Ridges

The seafloor of the North Atlantic Ocean is divided by a mid-ocean ridge system consisting of two diverging plate boundaries, respectively the North American plate and the Eurasian plate (Dubinin et al., 2013). The part of the plate boundary north of Iceland is known as the Arctic Mid Ocean Ridges (AMOR), a mid-ocean ridge system consistent of several ridge segments (from south to north); The Kolbernsey Ridge, the Mohn's Ridge, the Knipovich Ridge and the Gakkel Ridge (Dubinin et al., 2013). The AMOR extends from Iceland and terminates at the Siberian Shelf in the Laptev Sea, and covers approximately 4000 km of mid ocean ridges (Pedersen et al., 2010b). Additionally, the ridge system hosts three major fracture zones; The West Jan Mayen Fracture Zone (71°N), the Spitzbergen Fracture Zone (79°N) and the Molloy Fracture Zone (79°N) (Pedersen et al., 2010b). These fracture zones are responsible for breaking up the ridge system, and separating the Mohns Ridge from the Knipovich Ridge as well as the Lena Trough from the Gakkel Ridge (Pedersen et al., 2010b).

Mid-ocean ridge systems are considered to be the biggest contributors to the magmatic activity on Earth (Soule, 2015). The diverging motion of continental plates causes an upwelling of the underlaying mantle, that will undergo de-compressional melting and erupt at the sea floor as magma (Soule, 2015). Furthermore, this movement is frequently associated with episodic fractionation of the seafloor, production of dikes and basaltic lava flows (Soule, 2015). These conditions provide a satisfactory environment for hydrothermal activity and therefore the development and disposal of sulfide deposits, hydrothermal vents, plumes, and sediments. During the last two decades, the AMOR has been a desired research location for the University of Bergen and its Center for Deep Sea Research (Pedersen et al., 2021). Several research cruises to the AMOR and surrounding areas have resulted in discoveries of new hydrothermal fields, core complexes and hydrothermal plumes (Pedersen et al., 2021). Figure 3.1 gives an overview of the known hydrothermal fields (both active and inactive), sulfide deposits, and hydrothermal plumes.
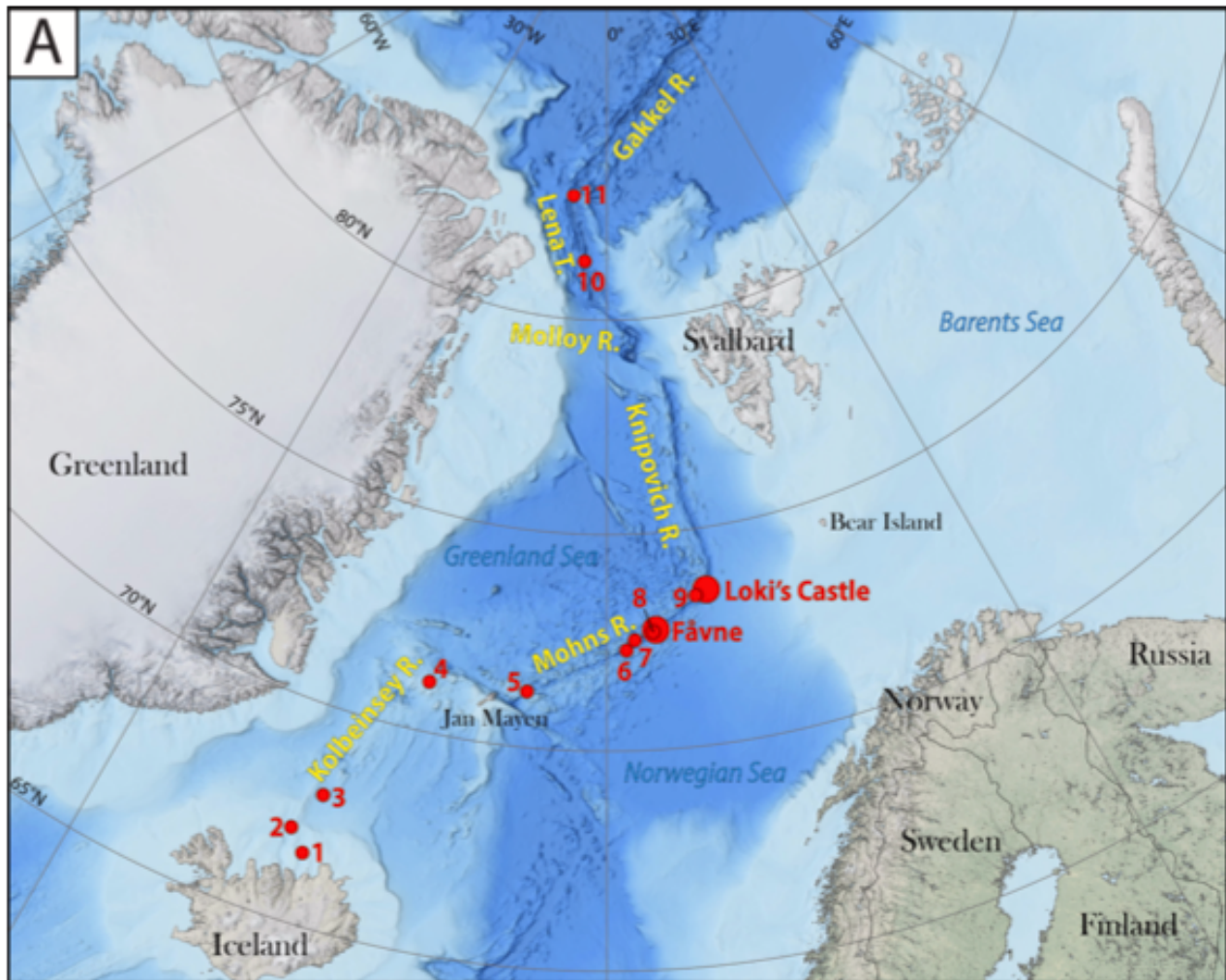
Figure 3.1: *Bathymetric map of sulfide deposits discovered at the Arctic Mid Ocean Ridge (AMOR).The red dots followed by numbers are the following fields; 1) Grimsey, 2) Kolbeinsey, 3) Squid Forest, 4) Seven Sisters, 5) The fields Soria Moria, Troll Wall and Perle & Bruse which belong to the Jan Mayen Vent Fields, 6) Ægirs kilde, 7) Copper Hill, 8) Gnitahei, 9) Mohns Treasure, 10) Lucky B, 11) Aurora. Fåvne and Loki's castle are marked with larger red dots as well as their respective names. Modified from (Sahlström et al., 2023).*

3.2 The Mohn's Ridge

The Mohn's Ridge is an ultraslow-spreading ridge, hosting both active- and inactive hydrothermal fields (Pedersen et al., 2010b). The southernmost part of the AMOR, including the Kolbernsey Ridge and the southern part of the Mohn's Ridge, is influenced by hot spot activity at Iceland and Jan Mayen (Pedersen et al., 2010a). Consequently, this area has an elevated topography and enhanced volcanic activity (Pedersen and Bjerkgård, 2016). Hydrothermal activity along the Mohn's Ridge has produced hydrothermal deposits such as the Jan Mayen Vent Field area (including the Troll Wall Field, Perle & Bruse Vent Field and the Soria Moria Vent Field), Copper Hill sulfide mineralization breccias, Ægirs Kilde Vent Field,

Mohns Treasure massive sulfides and the Loki's Castle Vent Field in the transition between the Mohn's ridge and the Knipovich ridge (Pedersen and Bjerkgård, 2016).

The samples in the following study were collected from hydrothermal vent sites along the AMOR on the Mohn's Ridge and the extension from the Mohn's Ridge to the Knipovich Ridge. The samples are from the vent fields Soria Moria, Fåvne and Loki's Castle. A representation of the sampling location for the three vent fields is shown on Figure 3.1. Loki's castle and Fåvne are marked with names on the map, whereas Soria Moria is located at point 5, which also includes the Perle & Bruse Vent Field, and the Troll Wall Vent Field.

3.2.1 The Soria Moria Vent Field

The Soria Moria Vent Field (71°15'N, 05°49'W) is situated on top of a volcanic ridge at approximately 700 meters depth, north-east of Jan Mayen, close to the Jan Mayen fracture zone (see Figure 3.1 for location) (Pedersen et al., 2010b) and is a part the Jan Mayen Vent Fields (Pedersen and Bjerkgård, 2016). The vent field is situated on the Mohn's Ridge and lays on top of one of the many volcanic ridges at the sea floor in this area (Pedersen et al., 2010b). The ridges are situated on top of an older lava field where large lava flows and lava tubes are deposited (Pedersen et al., 2010b). Two main vent areas were discovered at this vent field, with numerous chimneys (Pedersen et al., 2010b), and the vent structures normally range from 8-9 meters tall, whereas some of them also reach up to 10 meters (Pedersen and Bjerkgård, 2016). It is proven to be a high temperature field, based on the vent fluid temperatures that reach approximately 270°C (Pedersen and Bjerkgård, 2016). The hydrothermal chimneys at the field are known for emitting high temperature buoyant white smoker fluids (Pedersen et al., 2005).

3.2.2 The Loki's Castle Vent Feld

In 2008 a new vent field called Loki's Castle was discovered along the AMOR (Pedersen et al., 2010a). The vent field is an active black smoker field located at 73°30'N and 8°E, where the Mohns Ridge extends into the Knipovich ridge (see Figure 3.1 and 3.2 for location). Loki's castle is located near the top of a 30 km long axial volcanic ridge (AVR), and is a sediment-influenced and basalt-hosted hydrothermal field (Steen et al., 2016). The AVR is situated in a valley at the

seafloor, and stretches to 1300 meters above the lowest part of the valley (Pedersen et al., 2010b). The venting in this area is associated with a 50-100 meter deep rift/fracture running along the crest of the volcano (Pedersen et al., 2010a). There are four active black smoker chimneys at the site; João, Menorah, Camel and Sleepy, which are all located on top of a mound of hydrothermal sulfide deposits (Pedersen et al., 2010a). The venting temperature in the area ranges from to 20 to 320°C (Jaeschke et al., 2012, Pedersen et al., 2010a). Both venting with black and transparent outflow is discovered, where the black outflows indicate high temperature venting and the transparent reflect the low temperature outflows (Pedersen et al., 2021). The low temperature venting area covers approximately 400 m², and is characterized by transparent outflow of approximately 20°C (Steen et al., 2016). This part of the field is often referred to as the Barite Field, as the chimneys in the area have high abundances of barite (Steen et al., 2016).
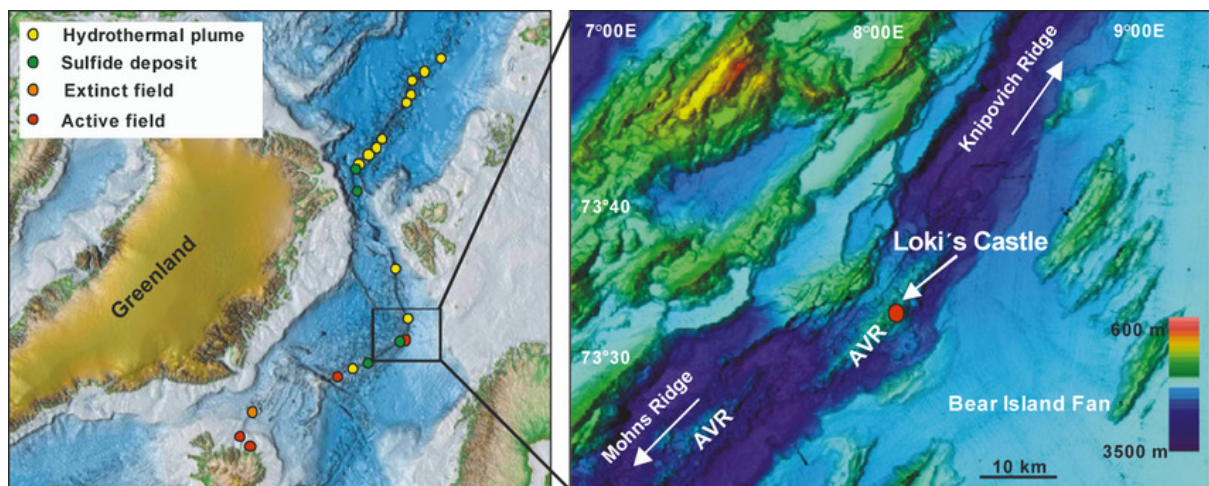
Figure 3.2: *Position of Loki's castle at the AMOR. Picture from (Jaeschke et al., 2012).*

3.2.3 The Fåvne Vent Field

The Fåvne Vent Field is a recently discovered active vent field located on the Mohn's Ridge, at 72.8°N, 4.2°E (see Figure 3.1 and 3.3 for location). It was discovered in 2018 at a cruise directed by the Norwegian Petroleum Directorate (NPD) (Pedersen et al., 2021). The field hosts both active and inactive vents and is mainly dominated by basaltic rocks. Approximately 700 meters from this vent field, an extinct sulfide deposit called Gnitahei is located (Brekke, 2021). Both Fåvne and Gnitahei are associated with a bounding fault at the NW flank of the Mohn's ridge, and Fåvne is located at the junction between the footwall and the hanging wall (Brekke, 2021). The chimney structures at Fåvne have black vent fluid outflow and the chimneys are therefore

characterized as black smoker chimneys (Brekke, 2021). The sample in this study is collected from the North Tower location at Fåvne (Figure 3.3).
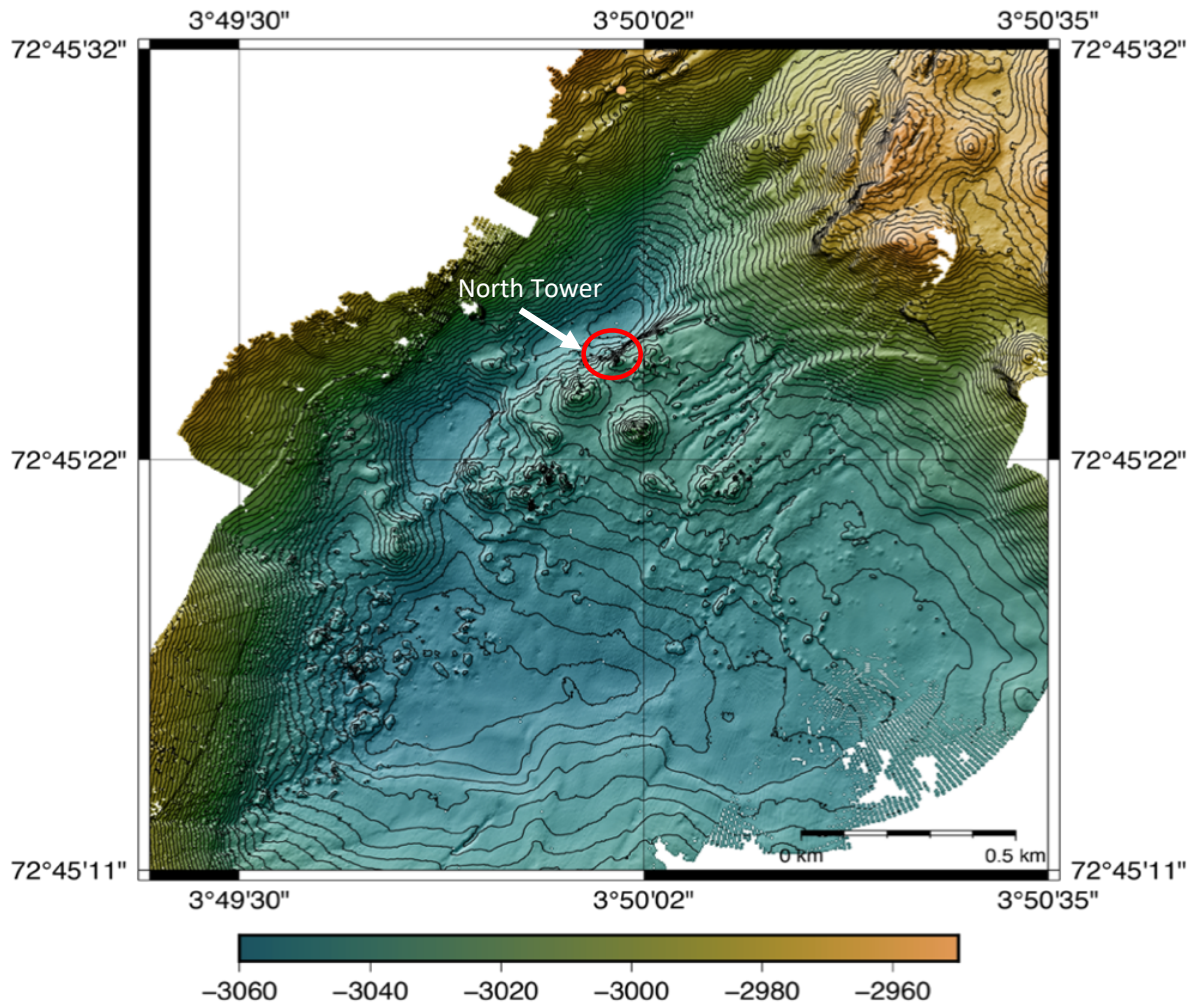
Figure 3.3: Bathymetric map of the Fåvne Vent Field. The North Tower area is marked in the red circle at the map. Modified from Centre for Deep Sea Research, University of Bergen.

4. Materials and methods

A visualization of the workflow conducted in the study can be found in Figure 4.3. A more detailed description will be provided in the following subchapters.

Figure 4.1: *Flow chart of the methodology walkthrough. Step by step: sampling at the seafloor, Raman spectroscopy, CT-scanning, preparation of thick sections, petrographic light microscope (PLM), scanning electron microscopy (SEM), Raman spectroscopy, image processing.*

4.1 Sampling and samples

The data presented in this thesis is based on samples collected during the annual research cruises performed by K.G. Jebsen Centre for Deep Sea Research in the years 2017, 2018 and 2019. These cruises were conducted using the G. O Sars research vessel, which is owned by Havforskningsinstituttet (75%) and the University of Bergen (25%) (Havforskningsinstituttet, 2022). During the cruises, rock samples were collected from the sea floor, multibeam echosounders provided sea floor bathymetry maps, gravity cores were taken, and additional geophysical data was acquired. All the samples in this project were collected by a remotely operated vehicle (ROV) at the seafloor. Table 4.1 gives an overview of the samples evaluated in the thesis, separated by the vent field they belong to, the coordinates in which they were collected, the associated water depth and the temperatures of the vent fluids at the vent site.

Table 4.1: Overview of the chimney from the study. The Fåvne chimney has not been named yet and is therefore added as the "North tower area", corresponding to its location. The depth is depth below sea level and temperature is the temperature of the fluids.

Sample ID	Chimney	Vent Field	Latitude	Longitude	Depth (m)	Temperature (°C)
GS17-ROV19-R03	Menorah	Loki's Castle	73°34.008'N	08°09.390'E	2314	316
GS18-ROV14-R01	Soria Moria	Jan Mayen	71°15.690'N	05°48.822'W	657	279
GS19-ROV16-R02	North Tower	Fåvne	72°45.408'N	03°50.016'E	3026	228

The Menorah chimney piece (Figure 4.2) is one of four active vent structures at the Loki's Castle Vent Field, as described in Chapter 3.2.2. It was collected during the G. O. Sars research cruise in 2017. The sample is approximately 10 cm tall and 3-5 cm wide.
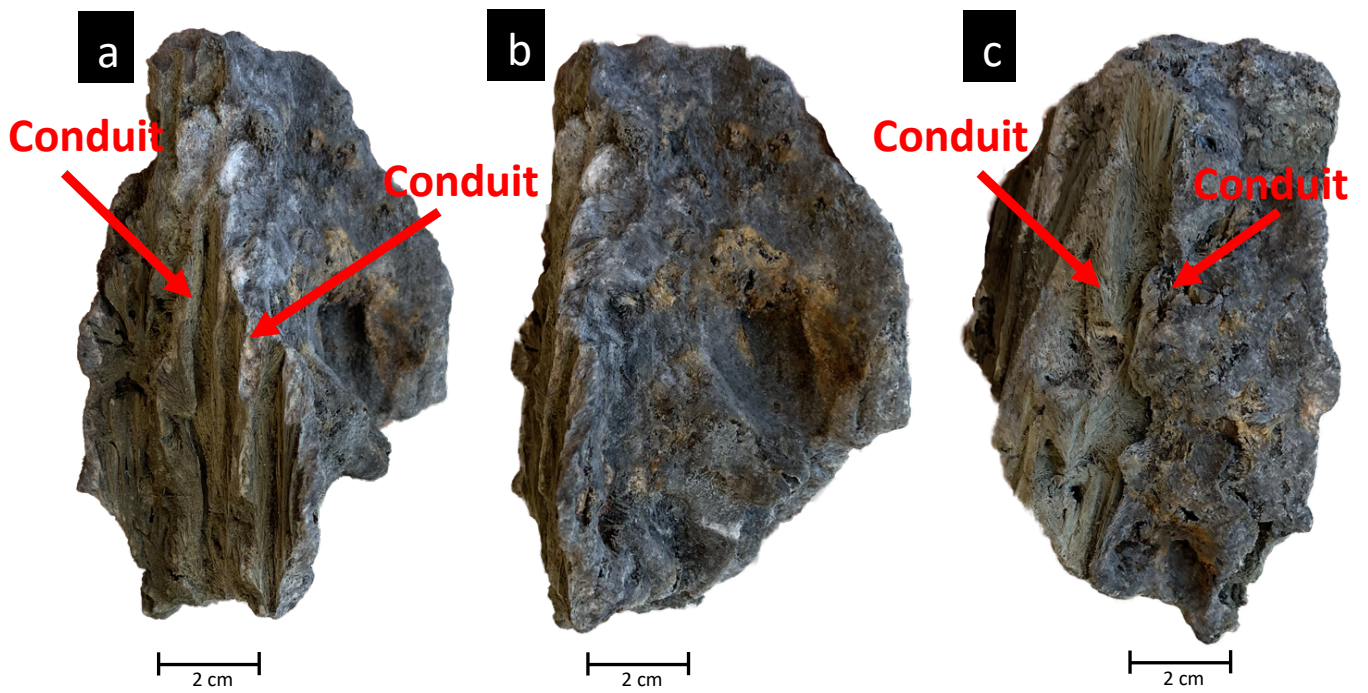
Figure 4.2: *The Menorah sample GS17-ROV19-R03 seen from 3 different angles. The pictures show conduits at the surface in figure 4.2a and figure 4.2c, see direction of arrows for visual representation of the conduits. Color differences on the surface indicate different minerals. Scale is approximate.*

The Soria Moria chimney (Figure 4.3) was sampled during the 2018 G. O. Sars cruise. It is a large chimney piece that is about 60 cm tall.
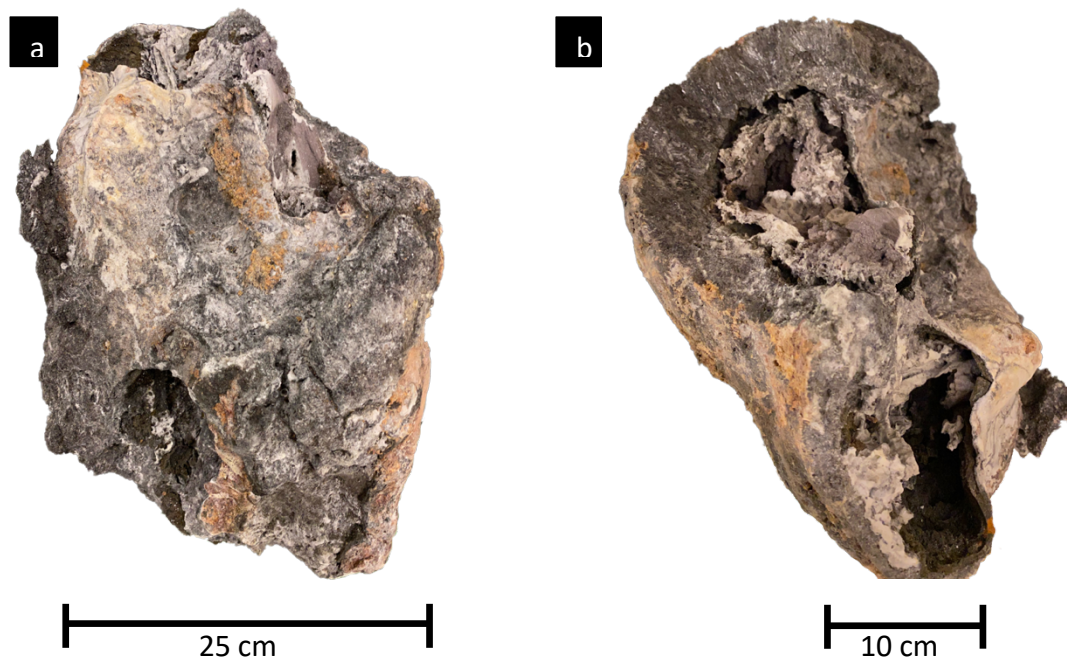
Figure 4.3: *The Soria Moria sample GS18-ROV14-R01 from one side (exposing the height) to the left (a) and from above to the right (b). Scale is approximate.*

The Fåvne North Tower chimney sample (Figure 4.4) was collected during the G. O. Sars research cruise in 2019. The chimney piece measure approximately 9 cm tall, and 2-4 cm wide. It has a conduit passing through the center of the chimney from the bottom to the top. The surface of the sample is covered in iron oxides.
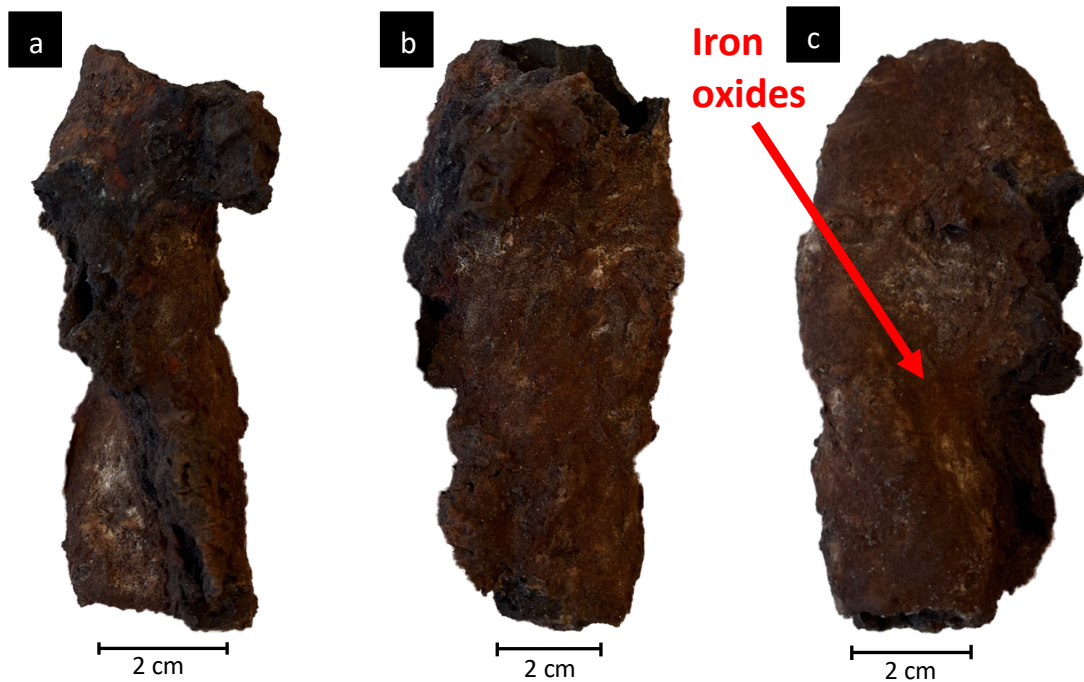
Figure 4.4: *The Fåvne chimney sample GS19-ROV16-R02 displayed from 3 different angles, giving a good representation of the morphology of the surface. Iron oxides are present on the surface of the sample as the sample has been oxidized (red arrow on on Figure 4.4c). Scale is approximate.*

4.2 Methods

4.2.1 Raman spectroscopy before CT-Scanning

The Raman Spectrometer at the Department of Earth Sciences at University of Bergen (UiB) is a Horiba LabRAM HR instrument (Figure 4.5). Raman spectroscopy uses wavelength difference (Raman shift) between incident and elastically scattered light to gain information about the nature of chemical bonds in the investigated material. The Raman shift can provide information about the chemical structure, phase, polymorphism, intrinsic stress/strain, contamination, and impurity (Horiba Scientific, n.d.). For the purpose of this study, a Raman spectrometer was used as a tool for identifying minerals. Spectra were collected using the 520 nm laser, and a 1800 gr/mm grating. To prepare for the CT-scanning (see chapter 4.2.2), minerals were identified by Raman spectroscopy, to be used as standards during CT-scans.

These were minerals expected to be present in the chimney samples, thus also minerals that reflect the same gray scale values, because of their density being the same. Minerals were picked based on earlier knowledge regarding minerals abundant in hydrothermal vents, and more specifically minerals proven to be present in the relevant vent fields. "Pure" minerals were collected from a rock sample storage in the basement of the Natural Sciences building at UiB and checked at the Raman afterwards. The Raman shift was derived from different minerals to confirm if the mineral was the same as expected. When results from the Raman spectrometer were retrieved, the obtained spectrums were compared with spectrums from the RUFF^{TM} Project database in CrystalSleuth.
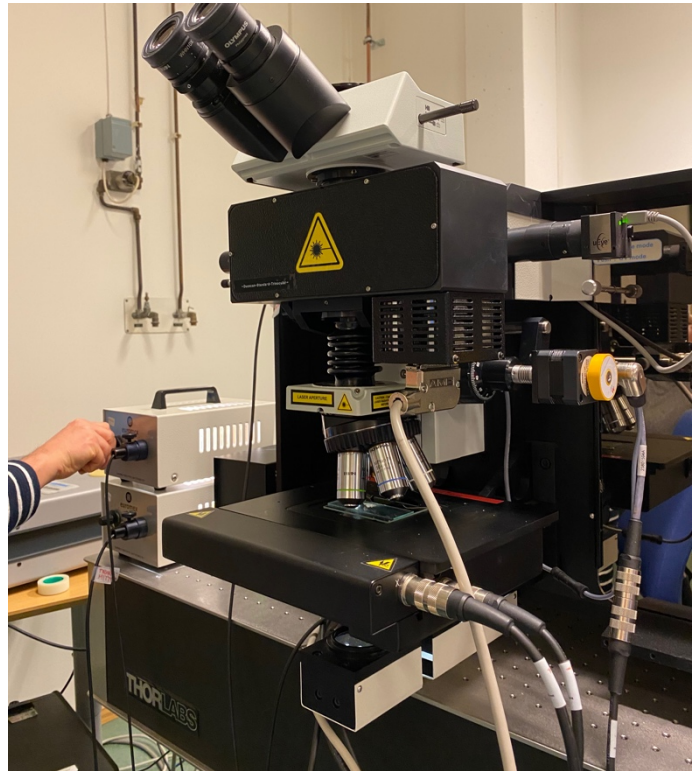
Figure 4.5: Raman Spectrometer on the 2nd floor of the Natural Sciences building at UiB.

4.2.2 CT-scanner

A ProCon X-Ray CT-ALPHA Computed Tomography (CT) scanner is based in the basement of the Earth Science Department at UiB. It belongs to the Earth Sciences Institute and is customized for scanning sediment cores, and therefore mainly used for that sole purpose. This means that the interior of the CT-scanner is specially adapted to cores with a setup where 1.5-meter-long sediment cores are attached to the base of the machine. During scans, the sample rotates while X-rays are directed at the sample, while a detector detects the X-rays. Three various chimney pieces were scanned, from respectively Soria Moria (GS18-ROV14-R01), Fåvne North Tower (GS19-ROV16-R02) and the Loki's Castle Vent Field (GS17-ROV19-R03). The two latter mentioned chimneys were of suitable sizes for the instrument and could therefore be scanned without performing comprehensive modifications to the setup (Figure 4.6 a). The Soria Moria chimney, however, proved too large for the original setup and thus a customized scanning setup was made using two large buckets (Figure 4.6b). Due to the size

and the need for modifying the setup, the Soria Moria chimney was the first chimney to undergo the CT-scan.
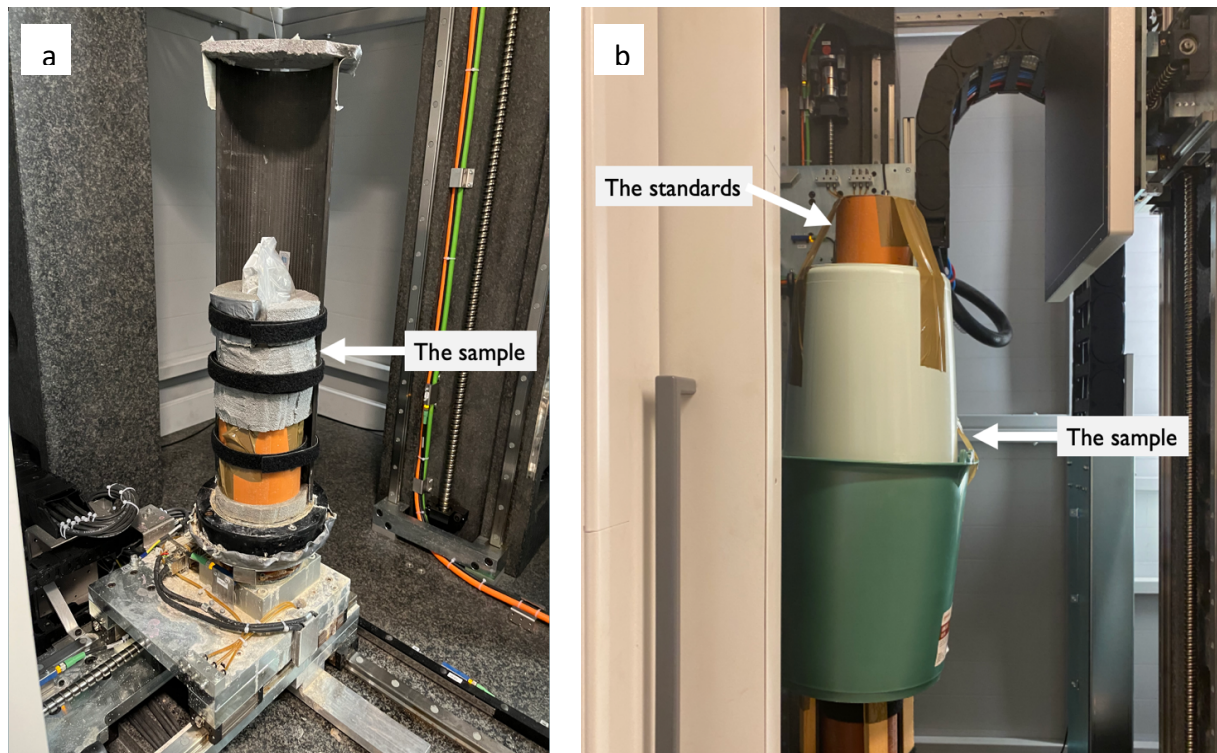
Figure 4.6: *(a) The picture visualizes the CT-scan setup for the Soria Moria chimney. The sample is placed in the green bucket which is screwed to a piece which again is attached to the CT-scanner. Thereafter another bucket is placed on top to create a stable surface for the standards. The standards are inside the brown pipe on top of the setup. (b) the setup used for the Menorah and the Fåvne chimney.*

The scanner employed in this study had never handled objects of this size, and thus had to be tested before moving on with the rest of the samples. As a measure for removing unwanted/unnecessary radiation inside the scanner during scans, it is equipped with a filter designed for absorbing the redundant radiation. The filter was changed depending on the material that was scanned, according to the size of the object and how much radiation that was expected. For all the chimneys scanned in this project, a copper filter was used – with varying thickness. As these chimneys, and especially the Soria Moria chimney, has a different size and mineralogical composition than the materials that usually are scanned in this CT-scanner, several scans had to be performed to get sufficient results.

A total of four scans were performed on the Soria Moria chimney. The need for several scans of this chimney is related to the quality of the data after the scans. The first three scans had a lot of streaking artifacts (Chapter 5.1 and 6.2 for detailed explanation), and some of them poor

resolution. The most satisfactory scan was the fourth and last one, which had good resolution and less streaking than the other scans. However only one scan was needed for both of the other chimneys. An overview of the settings for each scan is provided in Table 4.2 below.

Table 4.2: The 6 different scans performed listed with the specific settings applied and the thickness of the copper filter.

Scan nr.	Chimney	Filter	Kilovolt (kV)	Microampere (μA)	Exposure time (ms)	Resolution (μm)
1	Soria Moria	1 mm copper	190	1112	267	93
2	Soria Moria	2 mm copper	210	900	500	93
3	Soria Moria	2 mm copper	176	780	1000	93
4	Soria Moria	3 mm copper	240	1200	500	93
5	Fåvne	1.5 mm copper	150	900	334	33
6	Menorah	1.5 mm copper	150	900	334	33

To obtain density contrasts in an object, the machine uses X-rays focused on the object (Hounsfield, 1972). The product of the scans are presented as grayscale values in a spreadsheet, wherefrom data can thereafter be displayed in 3D and 2D through subject-specific software such as Avizo.

4.2.3 CT Processing

Data revived from the CT-scans was processed using the Avizo™ software provided by Thermo Scientific™ for image analysis and visualization (Thermo Fisher Scientific, 2018). For the purpose of this project, the Avizo™ 9.1.1 was used to process the CT data. The software was operated after completing CT-scans with the goal of producing 3D-models of the chimneys and interpret the mineral populations and abundances present. Grayscale data from the scans were imported to Avizo, where they display as voxels. Voxels are three dimensional pixels. They are put together to display the X-ray grayscale data in 3 dimensions. The dataset contains ortho slices of each "layer" of voxel-points, in x, y and z direction, that together are used to create 3D reconstructions of the data. The user guide provided by Thermo Scientific, was used as instructions for completing every step of the interpretations (Thermo Fisher Scientific, 2018).

The segmentation workroom in Avizo was used for creating 3D-models of the chimneys. Full 3D models of the chimneys Fåvne and Menorah were produced by interpreting the chimney material at approximately every 5th ortho slice in the y-direction and interpolating the material in-between the interpreted slices and adding it to a material in the segmentation main panel. Thereafter an interpretation of the present (mineral) populations in both datasets were conducted. As the datasets were large, only a few centimeters of each chimney were interpreted for mineral abundances. The data from both Menorah and Fåvne was therefore cropped to smaller pieces in the project view workroom, before the cropped version was opened in the segmentation workroom where interpretations were applied. Interpretations were done based on thresholding. Separate (mineral) populations were identified and added to a new model. After all the populations had been identified and added to the list of materials, they could be visualized in the 3D viewer. These new models were then visualized in the project room, where images for Chapter 5, were taken. Furthermore, ortho slices from the scans were extracted from Avizo with the purpose of comparing them to the mineralogical work. Ortho slices in the y direction were localized in terms of where thick sections were made.

4.2.4 Preparation of samples

To proceed with mineralogical studies of the chimneys, they were cut into thick sections. Each chimney was cut in 3 sections, one at the top, middle and bottom of the chimneys – in an attempt to represent the chimney throughout. The goal of the further study was to determine the minerology of the sample, from the bottom to the top of the smoker, ending up comparing the mineralogic analysis with the CT-scanned data. Before creating thick sections of the samples, they were cut by a wire saw where the Fåvne chimney piece was cut into 6 pieces (Figure 4.7), whereas the Menorah chimney piece was cut into 5 pieces (Figure 4.8).

Figure 4.7: The Fåvne chimney after cutting it with the wire saw. The thick section Fåvne first piece is from the 1 piece to the left, whereas the Fåvne middle piece is from the third piece from the left is and the Fåvne third piece is from fifth piece from the left. The thick sections will be presented in Chapter 5.4 (Figure 5.13, 5.14 and 5.15).

Figure 4.8: The Menorah chimney after cutting it in 5 pieces with the wire saw. The thick sections Menorah edge 1&2 are from the first piece from the left, Menorah middle 1, 2 & 3 is the third piece from the left, and Menorah top 1 & 2 is the last piece from the left. The thick sections of Menorah edge 1&2, Menorah middle 1,2 & 3 and Menorah top 1 & 2 are presented in the figures 5.16, 5.17 and 5.18 in Chapter 5.4.

After cutting the samples in chunks, the next step was to produce thick sections. Due to the fragile state of the chimney pieces, they were firstly molded in an epoxy resin before being cut to thick sections. The three Fåvne samples were placed in 3 separate containers and epoxy was poured over. The three Menorah samples were bigger than the Fåvne pieces and had to be cut in smaller pieces before molding them. Menorah edge was cut into menorah edge 1 and 2, Menorah middle was cut into Menorah middle 1, 2 and 3 and finally the Menorah top piece was cut into Menorah top 1 and 2. After the menorah pieces were small enough to fit on a thick section glass, they were also molded like the Fåvne samples. The samples stayed in the molds for 24 hours to ensure that the epoxy had solidified. Thereafter they were removed from the molds and thick sections were made. Each sample was then glued to the frosted side of a thin section glass, to prepare them for being cut. Followingly they were one by one

mounted to a rotary saw, with settings to cut the sections approximately 2 mm thick. Finally, the samples were polished to give a clean finish to the surface of the thick sections (See chapter 5.4 for thick sections). The Fåvne thick sections were named Fåvne first piece, Fåvne middle piece and Fåvne third piece (Figure 5.13, 5.14 and 5.15), and the Menorah samples were named Menorah top 1 & 2, Menorah middle 1,2 & 3, and Menorah Edge 1 & 2 (Figure 5.16, 5.17 and 5.18).

4.2.5 Petrographic Light Microscope

A petrographic light microscope was used to get an overview of the minerals present in the samples. The microscope was Nikon Eclipse LV100POL with a Nikon DS-F3 camera attached. As the material of interest was very fragile, thick sections were the only possibility for studying the samples. One of the main limitations to using thick sections, rather than thin sections, is that the material is too thick for the light to pass through, hence only reflected light microscopy can be applied. Opaque minerals, however, can be studied by using reflected light mode as transmitted light will make them opaque. As the minerals in the sample were hard to determine, scanning electron microscopy and Raman spectroscopy had to be used as supplementary analysis.

4.2.6 Scanning electron microscope (SEM) – Energy Dispersive X-ray spectroscopy

A scanning electron microscope is an instrument that uses electrons to assemble chemical characterization and analysis of individual elements. Electrons are used to produce images of a sample contrary to using light rays (Luyk, 2019). The samples must be conducting to produce results, as they have to be conducting. For this reason, a thin carbon layer is coated on top of each sample before starting analyses. A map of each thick section was produced at the SEM by creating high resolution backscattered images. Backscattered images give an overview of the samples presented in grayscale, where lighter colors imply higher density, and darker colors imply lower density, relative to one another. These maps were used as a tool for deciding where to do element mapping. Element mapping can be applied to areas of interest to determine the elements of interest in the area. However, exact minerals cannot be determined by the element mapping.

4.2.7 Raman spectroscopy after microscopy and mineralogical analysis

After CT-scanning, optical microscopy and SEM analysis are applied to the samples, some minerals are still unidentified. The results of the SEM analysis give an indication of the minerals present in both the Menorah and the Fåvne chimneys. The element mapping done at the SEM cannot detect water or carbon (as the samples are carbon coated), nor can it distinguish between for example pyrite and pyrrhotite, as they have the same chemical formula. As EDS-element mapping at the SEM gives chemical elements present in chosen areas, the Raman spectrometer was used to determine which exact minerals were present. The most common minerals associated with hydrothermal deposits, and their respective densities are listed in Table 4.3.

Table 4.3: Overview of the most common minerals associated with hydrothermal deposits. Listed according

ding to their respective densities.

Mineral	Formula	Density (g/cm^3)
Silica (amorphous)	SiO_2	2.65
Anhydrite	$CaSO_4$	2.97
Isocubanite	$CuFe_2S_3$	3.93
Sphalerite	$(Zn,Fe)S$	4.05
Chalcopyrite	$CuFeS_2$	4.19
Barite	$BaSO_4$	4.48
Pyrrhotite	$Fe_{0.08-1}S$	4.61
Marcasite	FeS_2	4.89
Pyrite	FeS_2	5.01
Iron oxides	Fe_2O_3	5.24

4.2.8 Image processing and thresholding

Backscattered image tiles from the SEM were processed by firstly stitching the tiles together, producing high resolution images of all the samples. To quantify the percentages of each mineral, individual tiles were thresholded using the Fiji Image J softtware. Thresholding is an imaging technique that uses image segmentation to quantify and visualize different materials in an image. The images in this case are converted from grayscale images to binary images consistent of only black and white, where the material of interest is white. After producing binary images for each separate material, the background is removed and the images are overlayed, a different color is given for each mineral. Thereafter the same approach is applied to the ortho slice images from the CT-scanner.

5. Results

5.1 CT-scanning and interpretation

5.1.1 Soria Moria CT-scan

Four scans were carried out for the selected chimney piece from the Soria Moria Vent Field, with an ortho slice form the last scan provided in Figure 5.1. Since this chimney proved difficult to scan in terms of the quality of the result, the final scan was just conducted at the upper part of the chimney, which measured a resolution of ~ 93 μm. The chimney was approximately 60 centimeters tall, whereas the scan covered only the top 20 centimeters of it. Figure 5.1 exhibits significant streaking artifacts that affects the ability to do further interpretations of the sample. At the left-hand side of the figure, there is a large conduit passing through the chimney. The air in the conduit and the air around the chimney reflected different gray scale values, even though they resemble the same material (see chapter 6.2 for further explanation).
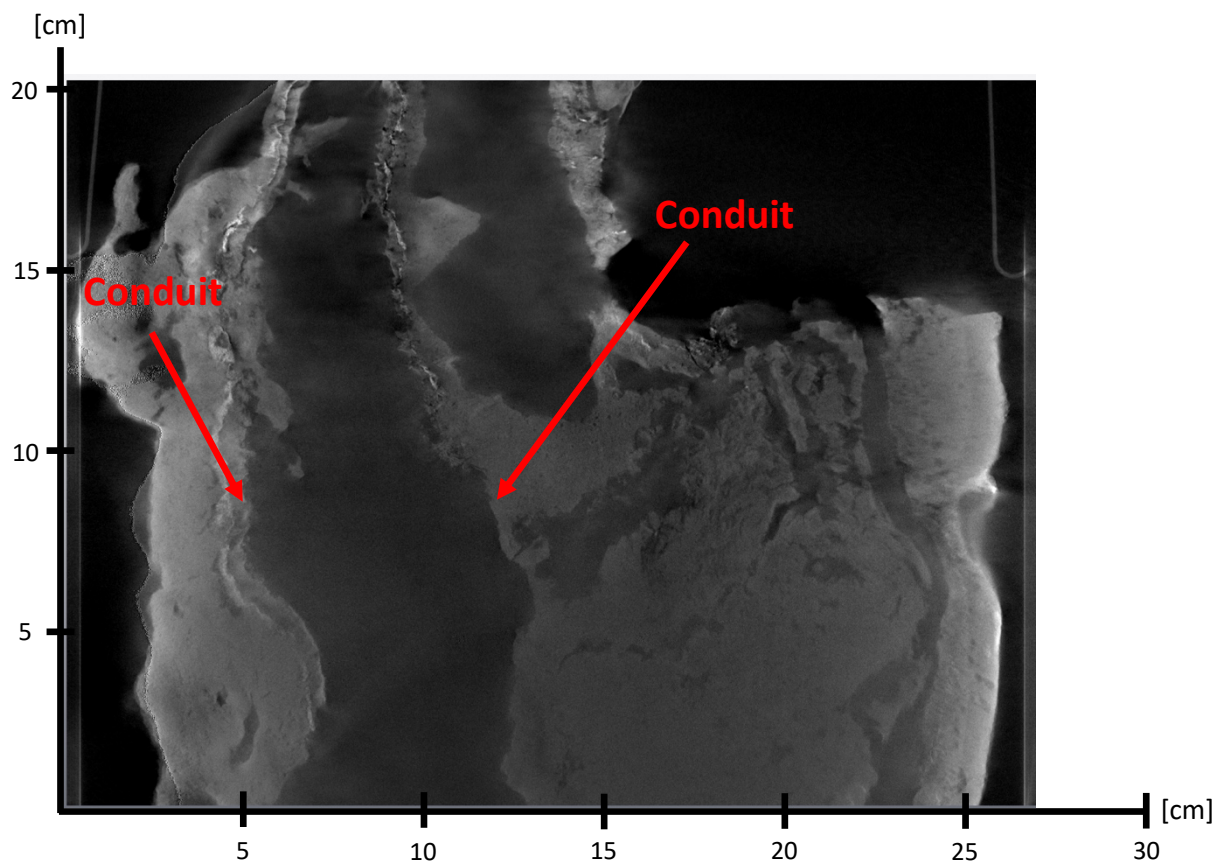

Figure 5.1: *The last CT-scan of the Soria Moria chimney from the side. The scan is showing high resolution, although visible streaking artifacts affects the density contrasts throughout the sample. Red arrows pointing to the conduit, which is the darker area between the two arrows.*

As some minerals were expected to be present in the chimneys, mineral standards were applied in the scans, to obtain a reference grayscale value that could be correlated with the grayscale values of the chimney, which could then help determine the minerals. The results of the scans with associated standards are shown in Figure 5.2 below. Even more streaking is apparent here, and the grayscale values of the standards compared to the mineral assemblages in the chimney shows no resemblance and is thus not used for the following part of the study.
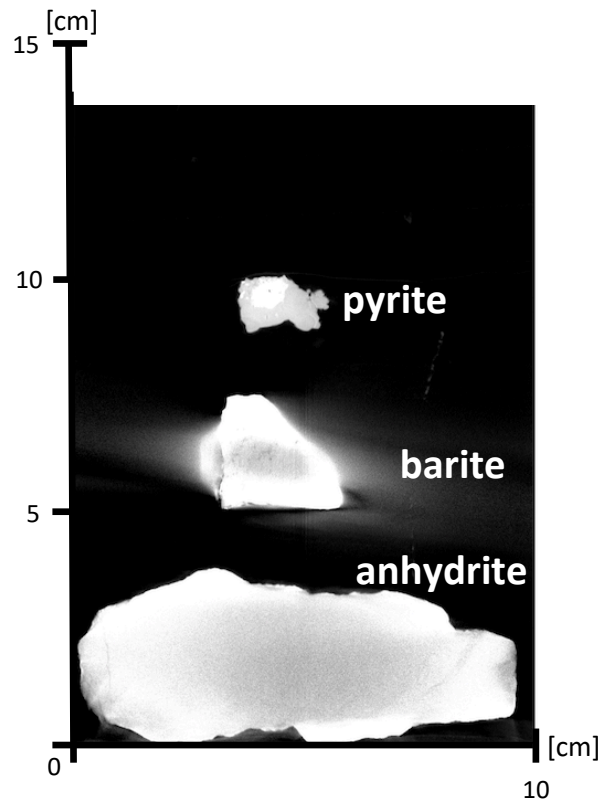
Figure 5.2: The figure shows the result of the 3D scan of mineral standards. From the top the minerals are pyrite, barite, and anhydrite.

5.1.2 Fåvne CT-Scan

The Fåvne 3D-model produced from the CT-scan data, display a visualization of the geomorphology of the chimney (Figure 5.3a, b, and c). After producing the 3D model, thresholding was applied to the datapoints as an attempt to interpret the mineral populations present in the chimney (see methods for details). A visual representation of the applied interpretation of different mineral/material assemblages is provided in a 3D model made up of voxels (Figure 5.4a), whereas the same interpretation of material is presented in an ortho slice (Figure 5.4b). The resolution of the Fåvne scan was ~33 µm (Table 4.2). As the dataset of this chimney was large, the lower few centimeters of the sample were chosen to interpret in terms of mineral populations (explained in Chapter 4.2.3). The thresholding interpretation resulted in 3 main density populations visualized in respectively brown, dirty white and yellow (Figure 5.4a&b). Inside of the chimney conduit, the streaking phenomenon mentioned in relation to the Soria Moria CT-scan reappears in the Fåvne chimney which affects the interpretations (Chapter 6.2 for explanation).
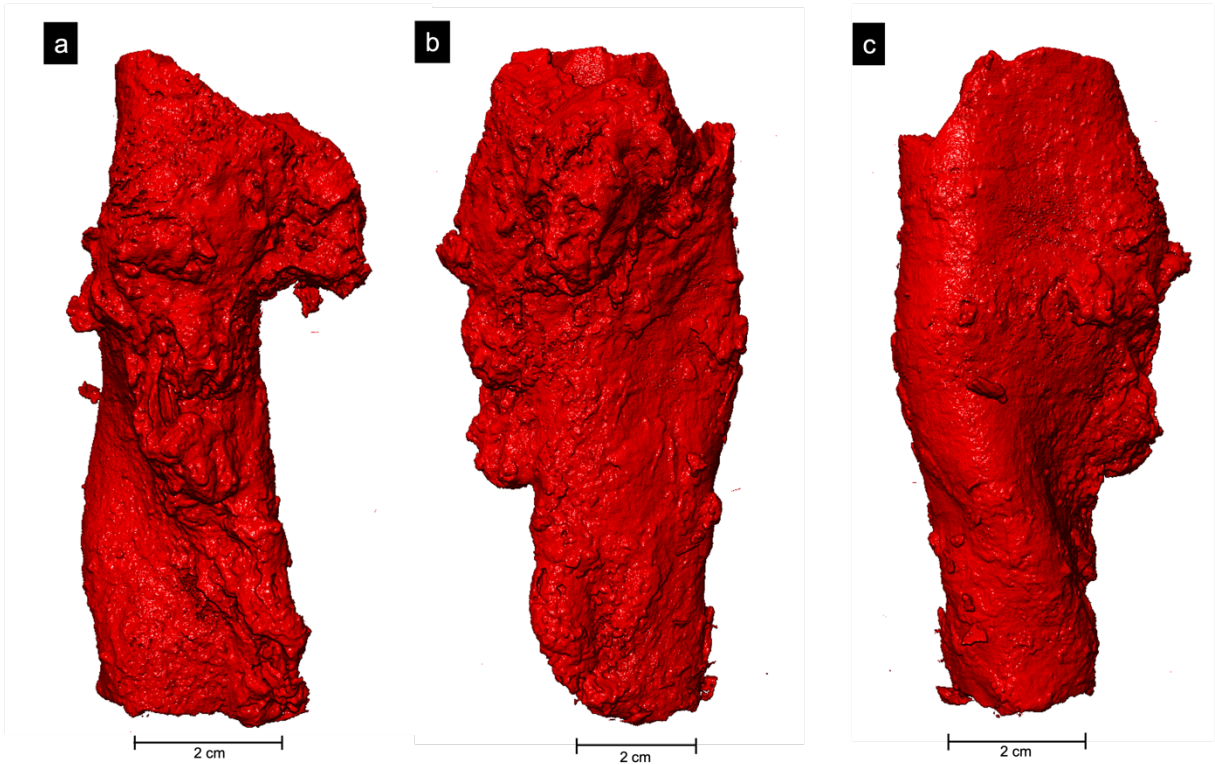
Figure 5.3: Produced 3-D model of the Fåvne North tower chimney from Avizo. a), b) and c) all represent the 3-D model from different angles.

Streaking artifact
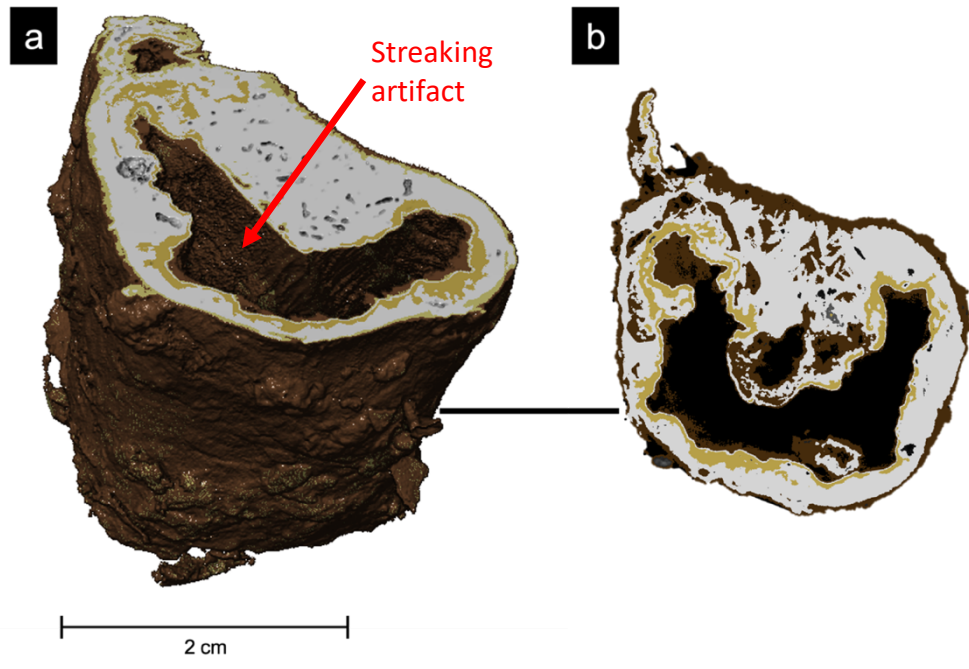
Figure 5.4: The figure displays a visual representation of the interpretations done with the grayscale data from the Fåvne North tower chimney piece. Grayscale interpretation revealed 3 clear differences in material density. Respectively, these are displayed in brown, dirty white and yellow. Figure 5.4.a is a 3D visualization of the interpretations of density differences, whereas figure 5.4.b is an ortho slice from the 3D model, displaying the area of Fåvne First Piece (one of the thick sections). Scale not persistent for both figures. The red arrow at Figure 5.4a is pointing to the brown layer inside of the chimney. This area is affected by streaking (See Chapter 6.2 for explanation).

5.1.3 Menorah CT-Scan

A 3D model of the Menorah chimney was also produced after the CT-scan. The resolution of the scan was ~33 μm (Table 4.2) and the interpretation results are displayed with varying angles (Figure 5.5 a, b, and c). Conduits that have transported fluids through the chimney are visible as depressions on the surface of the sample (Figure 5.5a and 5.5c).
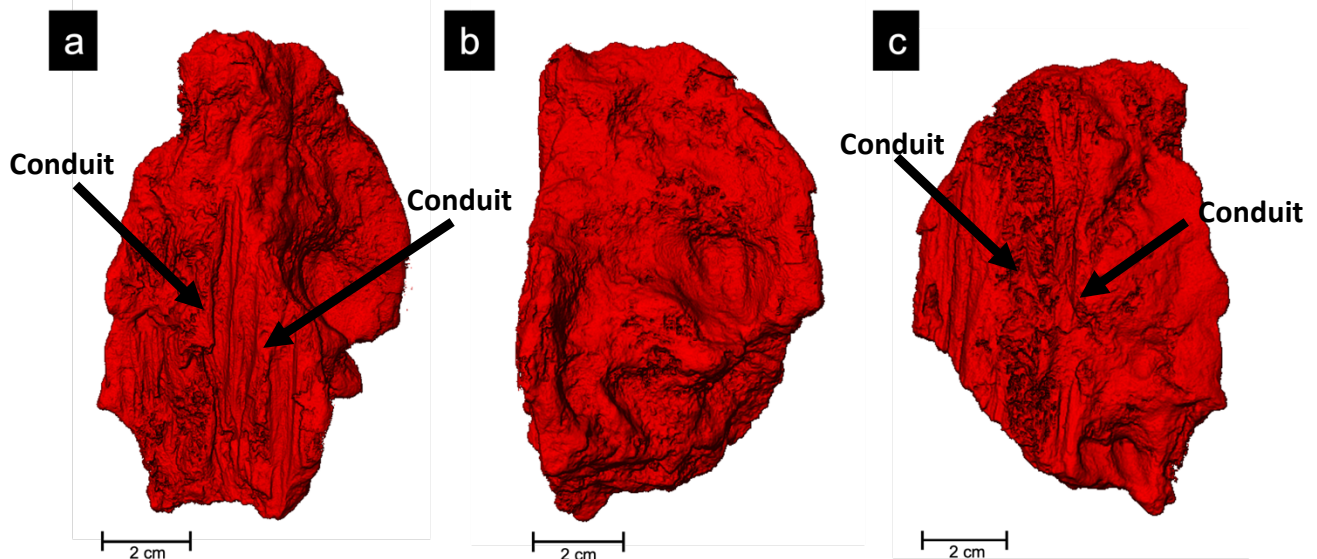
Figure 5.5: *Visualization of the processed CT-data, given in a 3D model in Avizo. Figure 5.5a and b indicates depressions at the surface, which can be related to fluid flow in the previous active vent. These are called conduits, and are shown with black arrows on figure a and b.*

The density contrasts in the Menorah chimney piece vary less than those of the Fåvne chimney piece, and consequently, the data was more challenging to interpret in Avizo. Figure 5.6 below is a visualization of the conducted interpretations. Since also this dataset was large, the lower few centimeters of this chimney were used for interpretations – like for the Fåvne chimney piece. The differences in density resulted in two identified main materials, both visualized in purple and green (Figure 5.6). The purple areas were the most dense material with the lightest gray scale color, whereas the green were the least dense material with the darkest grayscale values. This scan exhibit less streaking in the pores inside of the chimney compared to the Fåvne scan – making the model easier to interpret in terms of scanning artifacts. The interpretations show that there were some troubles with distinguishing between air and solid material in the areas around the edges of the chimney, as well as in conduits and/or pores within (Figure 5.6). The material "floating" in the air next to the chimney is the plastic bag that

was around the chimney during scans (Red arrow Figure 5.6a). Since the plastic has the same density as the green material, it was difficult to remove during interpretations.
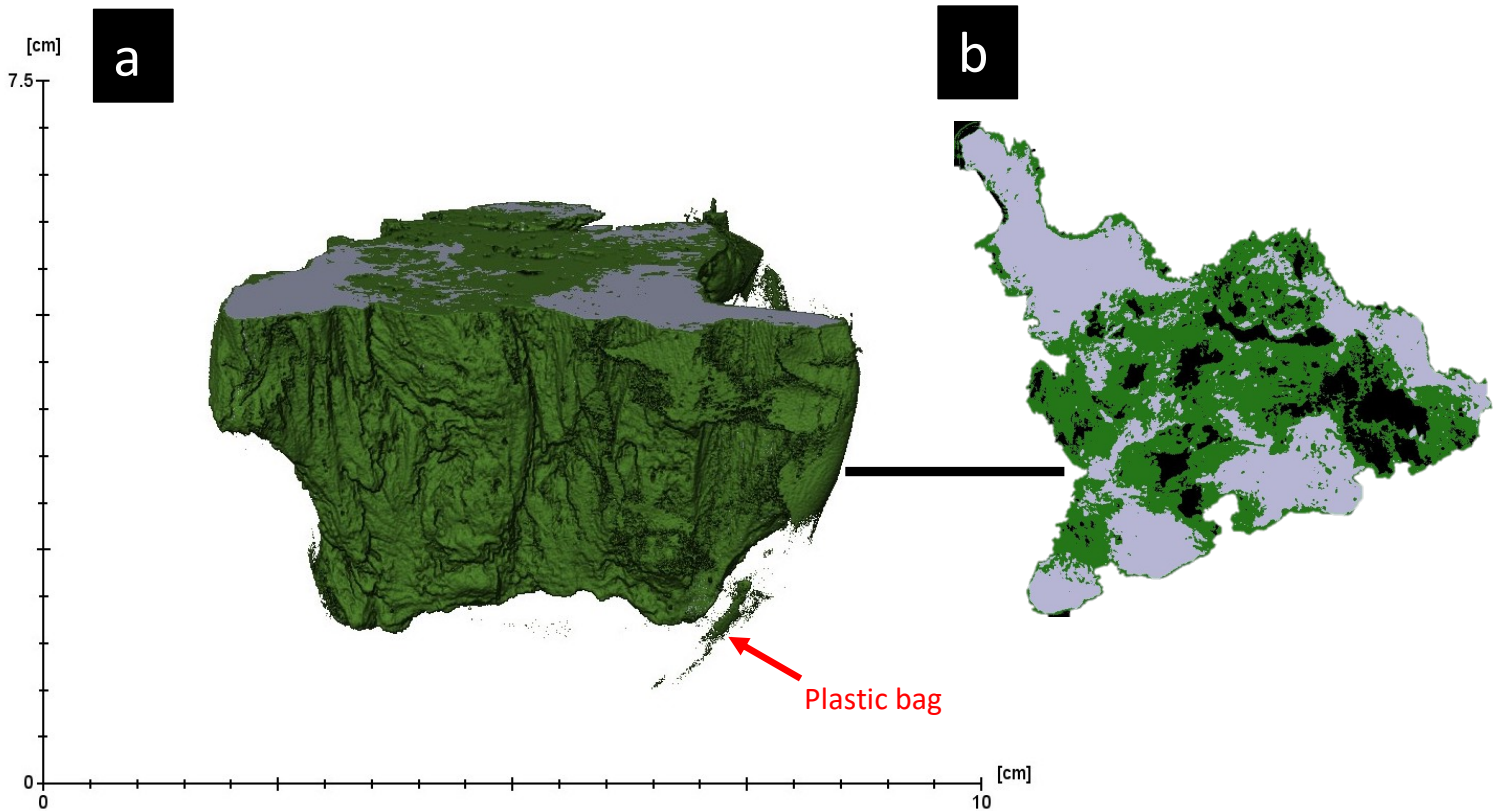
Figure 5.6: *3D-interpretation of the Menorah chimney. The green material on the figure represents the lightest material, whereas the light purple represents the heavier material. As the density contrasts are not easily apparent in this sample, two main materials are assumed present. Red arrow pointing to the area where the plastic bag is exposed in the interpretation. Scale not persistent for both figures (a&b).*

5.2 Ortho slices – Avizo

3D-models can as be visualized and produced in Avizo, as forementioned (Chapter 5.1). Each layer building the 3D-vizualization can be visualized separately in both x, y and z direction. These individual layers are called ortho slices. After finishing the production of 3D-models in Avizo as well as the mineralogical work, the thick section produced for mineralogical work were located in Avizo.

5.2.1 Fåvne ortho slices

Ortho slices made in Avizo are used to visualize the three areas sampled for 2D analysis as well as the interpreted version of Fåvne first piece (Figure 5.7a). The uninterpreted ortho

slices in Figure 5.7b, 5.7c and 5.7d represent the thick sections Fåvne first piece, Fåvne middle piece and Fåvne third piece respectively (which will be presented in Chapter 5.4.1). The scan was good enough to reconstruct the chimney and to identify the major density differences. The streaking artifacts (Chapter 5.1.2) were less prominent in the ortho slices (compared to the interpretations Figure 5.4), however they were problematic during interpretations. The significant hole in the middle of the chimney indicates a path where the fluids have migrated during precipitation of the minerals in the vent structure. A solid rock is surrounding the conduit in which a layered structure is visible from the inside and outward (Figure 5.7). The grayscale differences suggest that there are different materials present throughout the chimney. Based on the gray scale imaging from the 3D model, 3 different materials were interpreted to be present in the chimney. The first material, from the inside and outward, was the material giving the lightest gray scale color – thereby also the heaviest (arrow 1, Figure 5.7b). The second material was the abundant gray color where large, elongated crystals are visible, which accounts for most of the vent structure (arrow 2, Figure 5.7c). Lastly there was a darker gray mainly at the outer rim of the chimney, representing the least heavy material (arrow 3, Figure 5.7d). These observed differences within the model are displayed in colors of yellow, dirty white, and brown respectively (Figure 5.7a).

5.2.2 Menorah ortho slices

Ortho slices from the Menorah chimney are distinctively different compared to ortho slices from the Fåvne North Tower chimney (Figure 5.8). The overall trend suggests that there were more, but smaller conduits creating pores in the vent structure. The difference in material was not as prominent as in the Fåvne piece, and therefore harder to interpret. Overall, the mineral crystals are smaller than those seen in the chimney piece from Fåvne. The most dense material covers the brightest gray scale values (arrow 1, Figure 5.8b), while the least dense material covers the darkest gray scale values (arrow 2, Figure 5.8b).
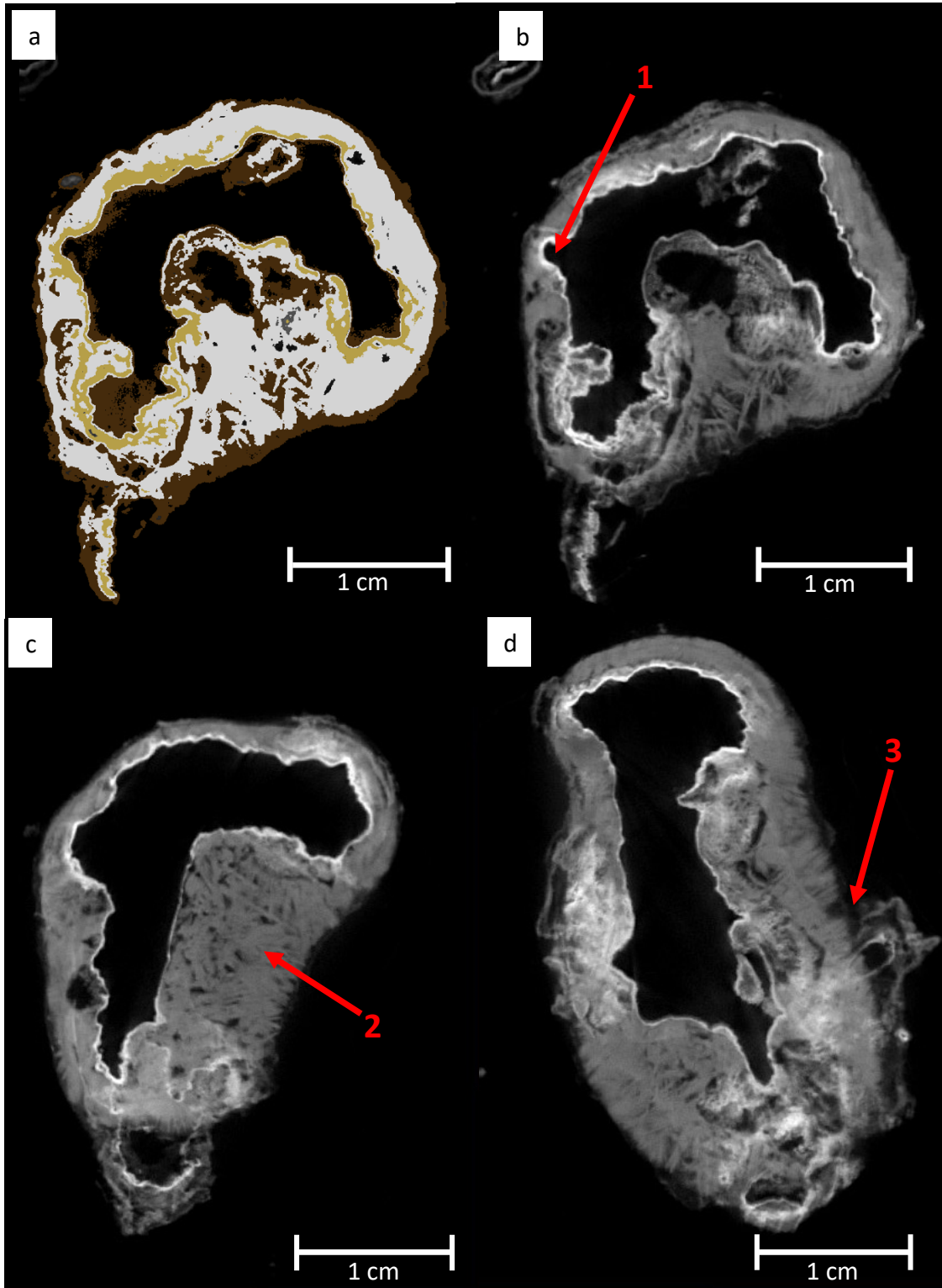
Figure 5.7: Ortho slices from the Fåvne North Tower vent. (a) Interpreted ortho slice of Fåvne first piece. (b) Ortho slice Fåvne first piece. Arrow 1 points to the most dense material (c) Ortho slice Fåvne middle piece. Arrow 2 points to the most abundant middle-gray material (d) Ortho slice Fåvne third piece. Arrow 3 points to the least dense material.
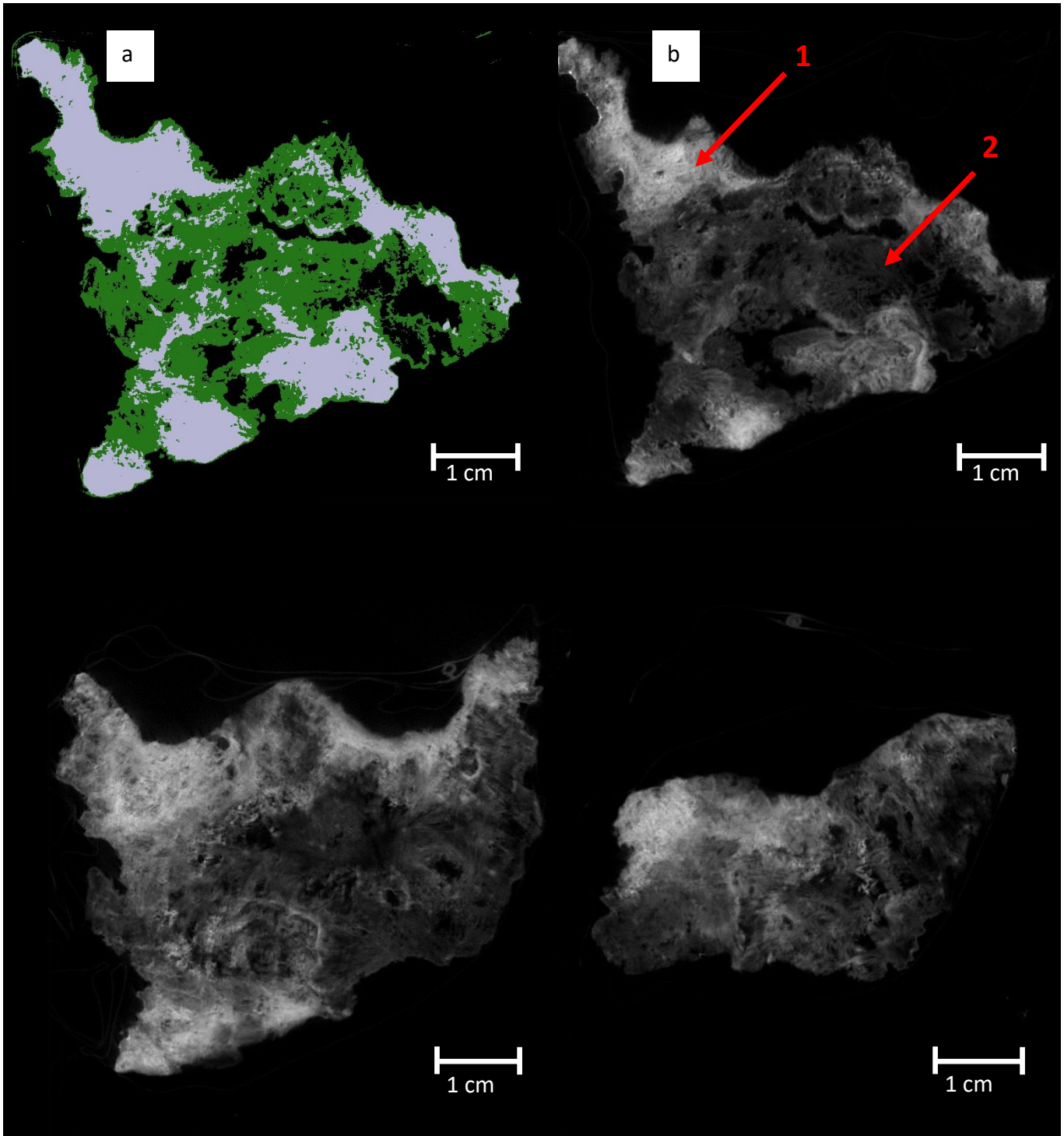
Figure 5.8: Ortho slices Menorah chimney. (a) Ortho slice Menorah edge with interpretation. Purple indicates the heaviest material whereas the lightest material is green, (b) Ortho slice of Menorah edge. Arrow 1 points to the most dense material, while arrow 2 point to the least dense material. (c) Ortho slice of Menorah middle. (d) Ortho slice of Menorah Top.

5.3 Optical microscopy and imagery

Thick sections with specified locations are visualized on the 3D-models in Figure 5.9.
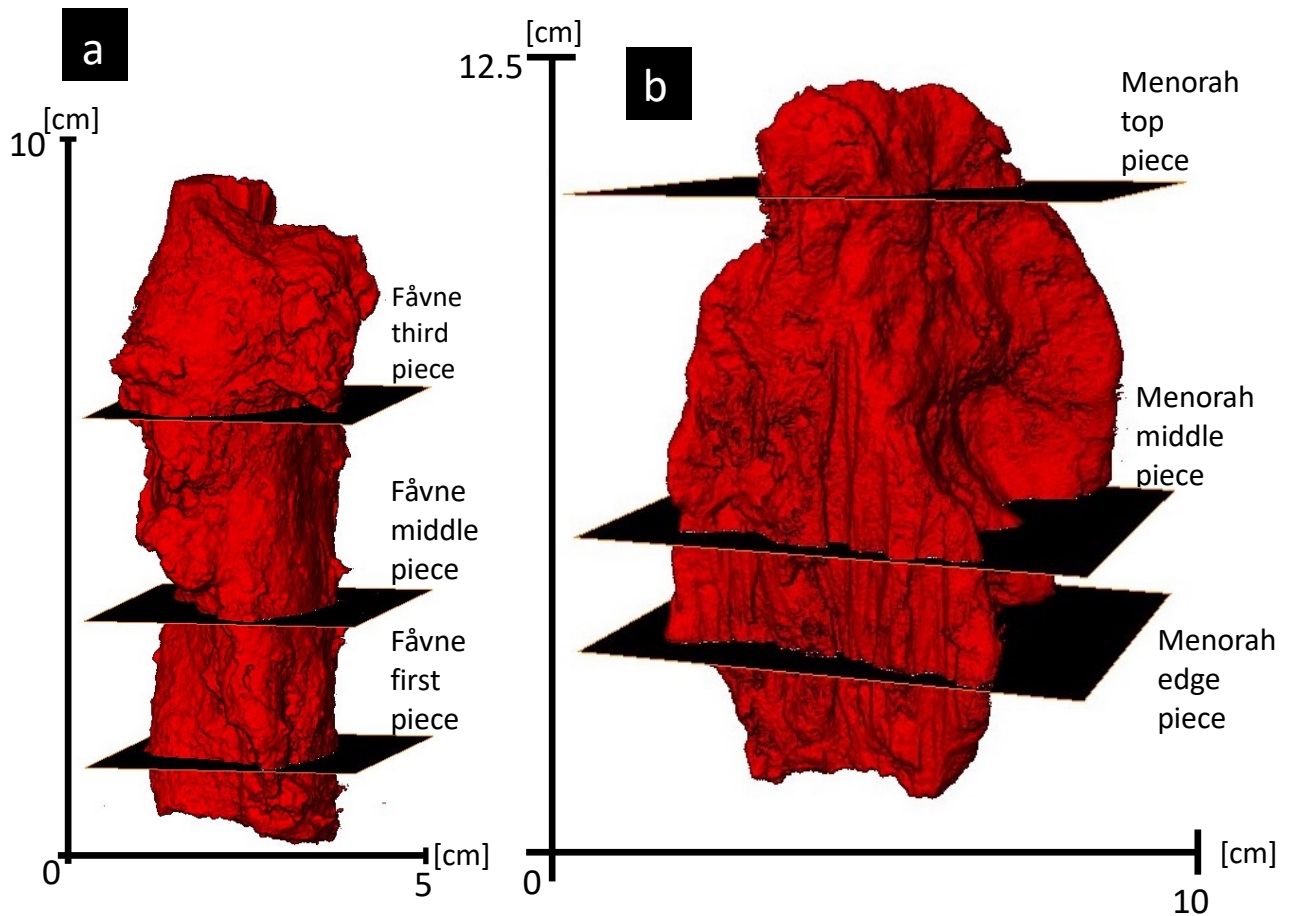
Figure 5.9: *Visualization of the locations where thick sections were made, marked with black sheets. a) Fåvne 3D model with locations of the 3 thick sections made. From the bottom Fåvne first piece is the first, Fåvne middle piece is the second and Fåvne third piece is the third. b) Menorah 3D-model with location of the thick sections made. From the bottom Menorah edge piece is the first one, Menorah middle is the second and Menorah top is the last*

5.3.1 Fåvne - optical microscopy and imagery

As some of the samples were too big for the thick section glass, they had to be cut in smaller pieces to be able to analyze the whole areas of interest. In the process of cutting these samples, some of the outer edges were lost, due to fragile state of the chimneys, size and inaccurate cutting. Optical microscopy on all thick sections was used as a measure for identifying the number of minerals present, and to have an overview before applying further mineralogical methods. As the samples were thick sections, only reflected light microscopy could be applied, as the samples were too thick to have light transmitted through the material.

Additionally, some of the expected minerals (sulfides) are opaque and can therefore not be studied in transmitted light anyway.

The vent structure from Fåvne has a prominent layering from the inner part of the chimney and outwards. This is consistent with the grayscale data from the CT-scan as well as the optical properties. Observations from reflected light microscopy suggest that there are 5 minerals present. An overview of the observations done in the optical microscope is given in the Table 5.1 below, as well as a visual representation of some of the observations on Figure 5.10.

Table 5.1: Overview of the findings from optical microscopy. Mineral 1, 3 and 5 can be seen in Figure 5.10 below.

Sample ID	Chimney	Minerals	Color in reflected light	Comment
GS19-ROV16-R02	Fåvne	Mineral 1	Yellowish gray	Small crystals
GS19-ROV16-R02	Fåvne	Mineral 2	Gray	Small crystals
GS19-ROV16-R02	Fåvne	Mineral 3	Dark gray (bit darker than nr 5)	Small subhedral crystals
GS19-ROV16-R02	Fåvne	Mineral 4	Blueish white	Oxidized after reacting with air over time
GS19-ROV16-R02	Fåvne	Mineral 5	Gray	Large euhedral crystals

.
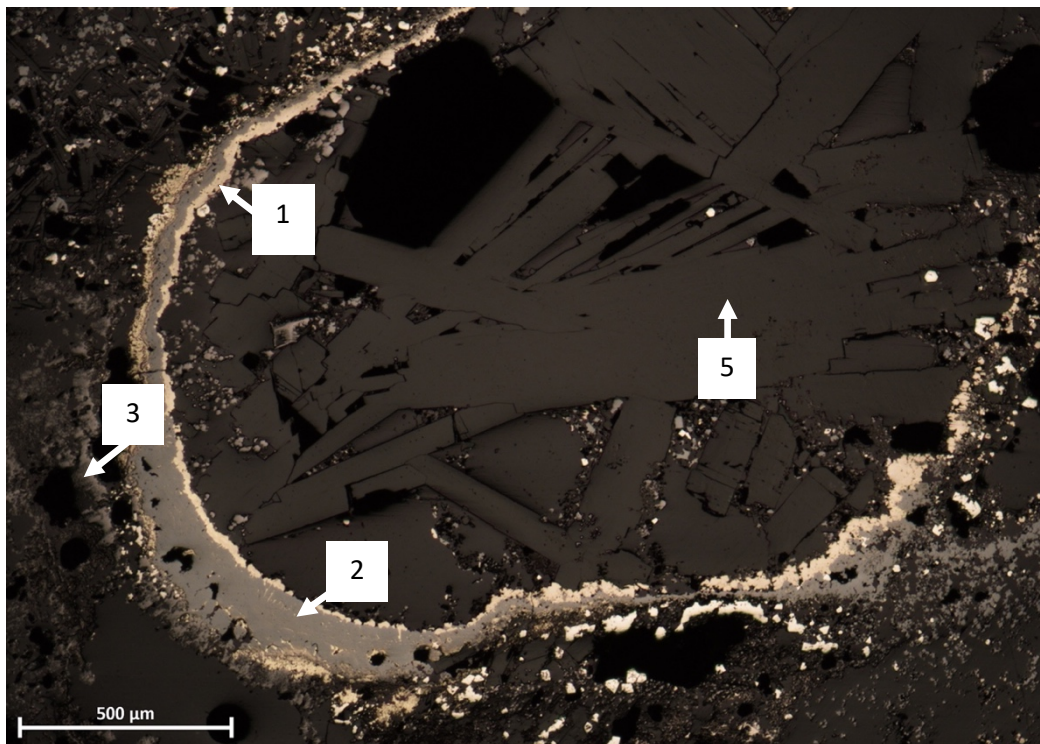
Figure 5.10: *Overview of the minerals identified after reflected light microscopy. The numbers refer to the description of the minerals found in Table 5.1 above. Mineral 3 is present as very tiny crystals, whereas mineral 4 is not seen in this photo.*

5.3.2 Menorah optical microscopy

The Menorah vent structure has, in contrast to the Fåvne chimney, more intergrown minerals instead of layering. Table 5.2 underneath is provided to give an overview of the minerals observed in the optical microscope. These analyses suggest the presence of five minerals, although some are too small to identify special features. Visual representation of the minerals can be seen in figure 5.11 and 5.12.

Table 5.2: The observed minerals have not yet been identified and are therefore just given a number. Mineral 1, 3, 4 and 5 can be seen in the Figures 5.11 and 5.12 below.

Sample ID	Chimney	Mineral nr	Reflected light
GS17-ROV19-R03	Menorah	1	Bright white
GS17-ROV19-R03	Menorah	2	Bright white
GS17-ROV19-R03	Menorah	3	Gray/light gray/transparent
GS17-ROV19-R03	Menorah	4	Light gray to yellowish white/gray
GS17-ROV19-R03	Menorah	5	Gray/brown/blueish brown
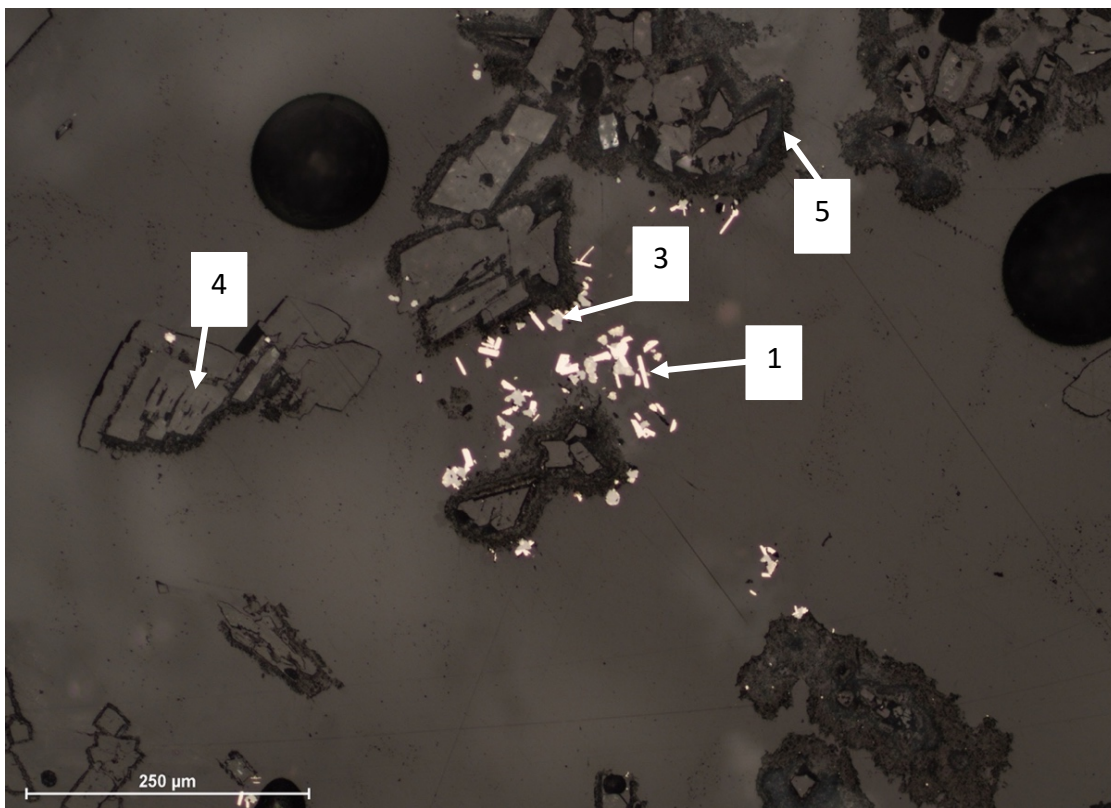
Figure 5.11: *Picture taken from Menorah top 1. An overview of the observed minerals in the chimney. Mineral 2 is not visible here. Display the size of most sulfides in this chimney.*
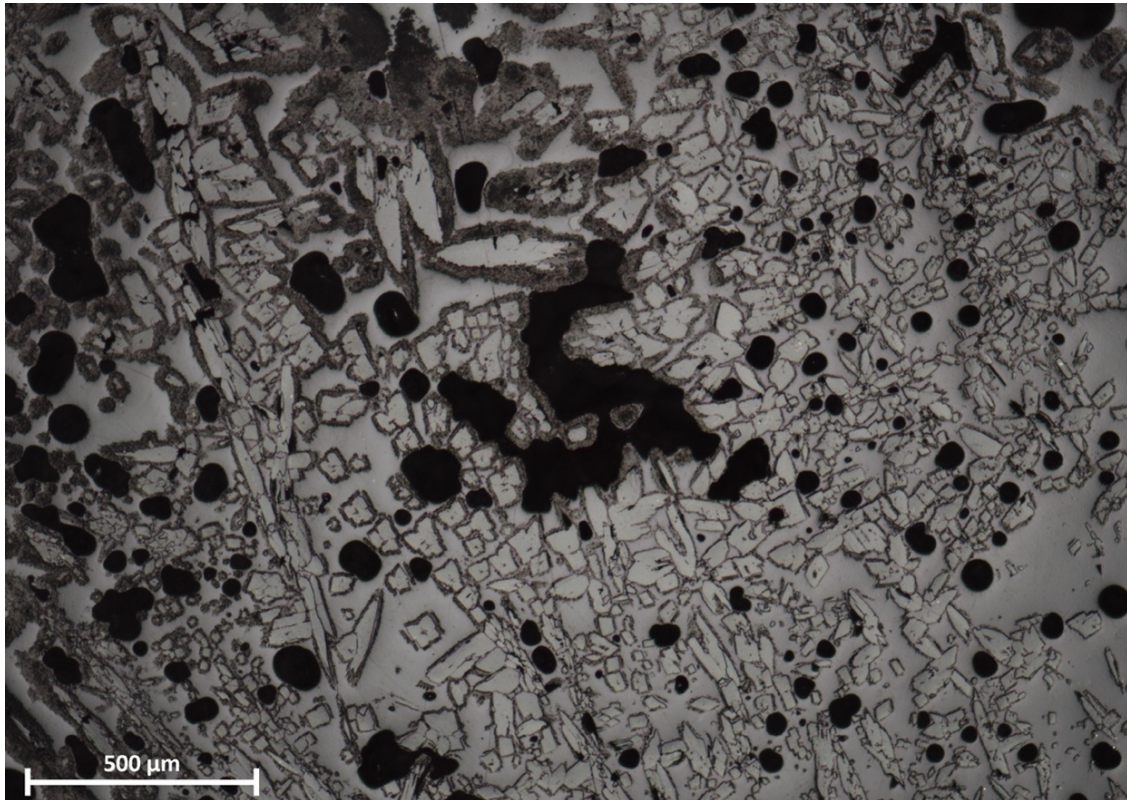
Figure 5.12: Taken from the same thick section as the picture in Figure 5.11. Mineral nr 4 and 5 are both very abundant. The black spots circles on the picture are bubbles from when the thick section was molded in epoxy.

5.4 Printer scans and SEM high resolution backscattered maps

5.4.1 Fåvne and Menorah

Prior to creating high resolution backscattered electron (BSE) maps at the SEM, regular printer scans were produced of each chimney sample (Figure 5.13a, 5.14a and 5.15a) – to be used as a tool for producing the backscattered maps afterwards. The printer scans provide real time colors and make larger crystals visible to the human eye. Small metallic crystals can be seen in various spots around the samples, especially toward the middle of the samples (Figure 5.13a, 5.14a & 5.16a). Longer bladed crystals can be noticed closer to the outer rim of the sample (Figure 5.13a, 5.14a & 5.16a).

The BSE maps from Fåvne North Tower provided high resolution gray scale contrast maps (Figure 5.13b, 5.14b and 5.15b). This is the "mineralogical" equivalent of the ortho slices from Avizo (Figure 5.7), where light grayscale colors indicate high density material and dark grayscale color indicate low density materials (such as air). The distinctive "Fåvne" layering is

also visible in these scans, whereas the heaviest materials are centered around the conduit and lighter materials moving further from the center of the chimney.

The same steps were repeated for the Menorah chimney. Prior to creating the high resolution back scattered maps, printer scans were made of each thick section and thereafter stitched together to provide full images of the whole chimney slices. The printer scans provided color differences throughout the samples along with crystal structures. On the contrary, the backscattered maps brought forward more detailed crystals along with density contrasts. The first scan is the sample Menorah edge (Figure 5.16), whereas the second scan is Menorah middle (Figure 5.17) and the last one is Menorah top (Figure 5.18). The BSE maps from Menorah represent the "mineralogic" equivalent of the ortho slices presented from Avizo (Figure 5.8).
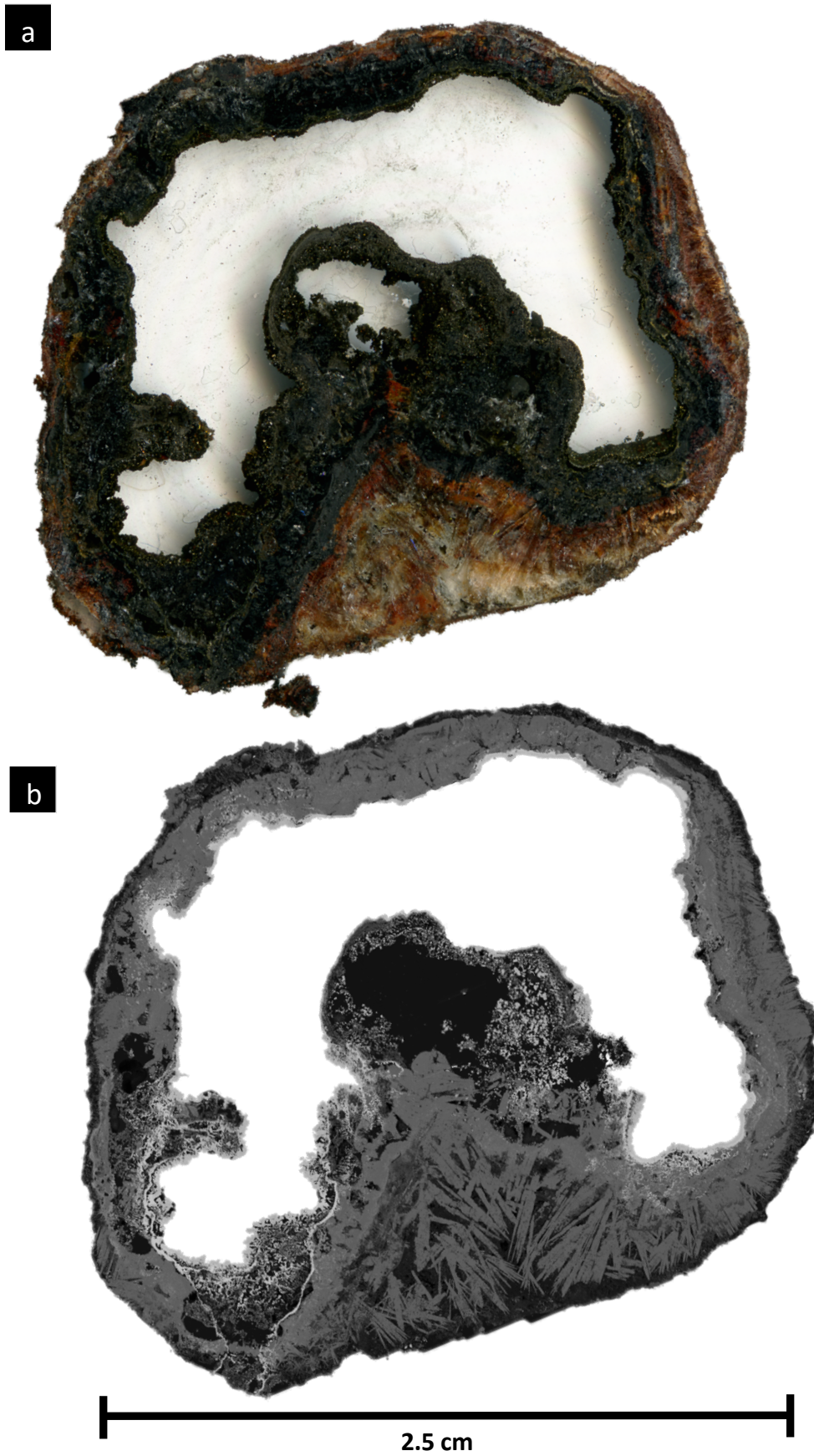
Figure 5.13: (a) Fåvne first piece printer scan. (b) High resolution back scattered map of Fåvne first piece. The scale is approximate.
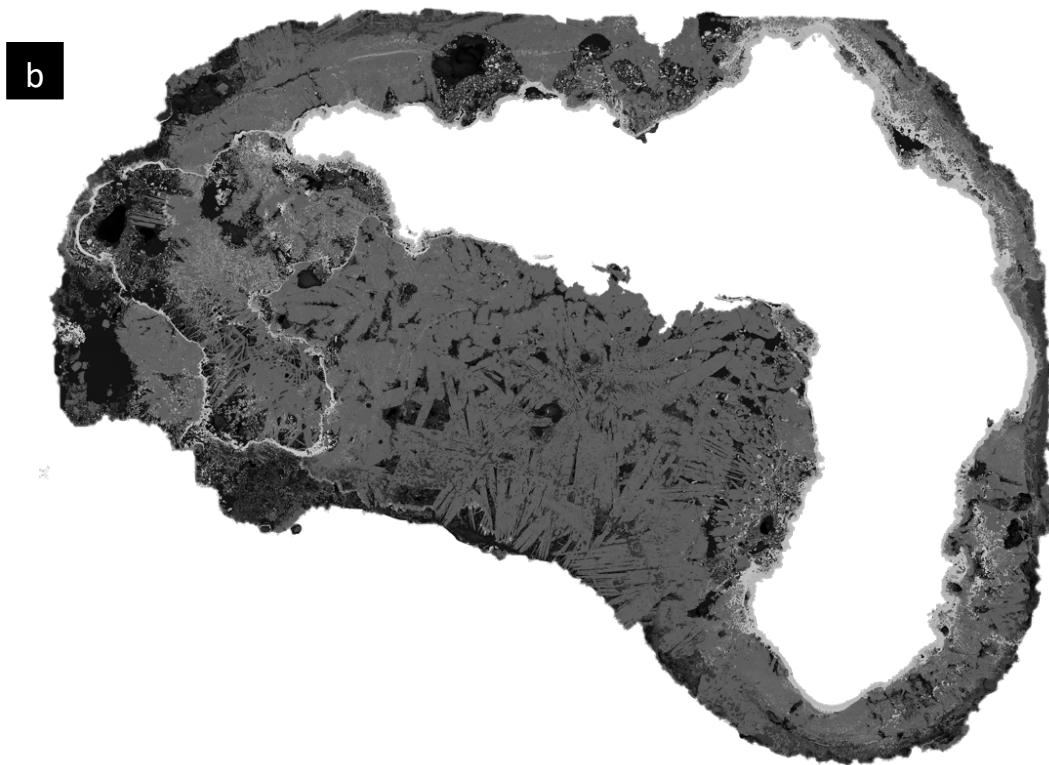
Figure 5.14: *(a) Fåvne second piece printer scan. (b) Fåvne second piece high resolution back scattered map. The scale is approximate.*
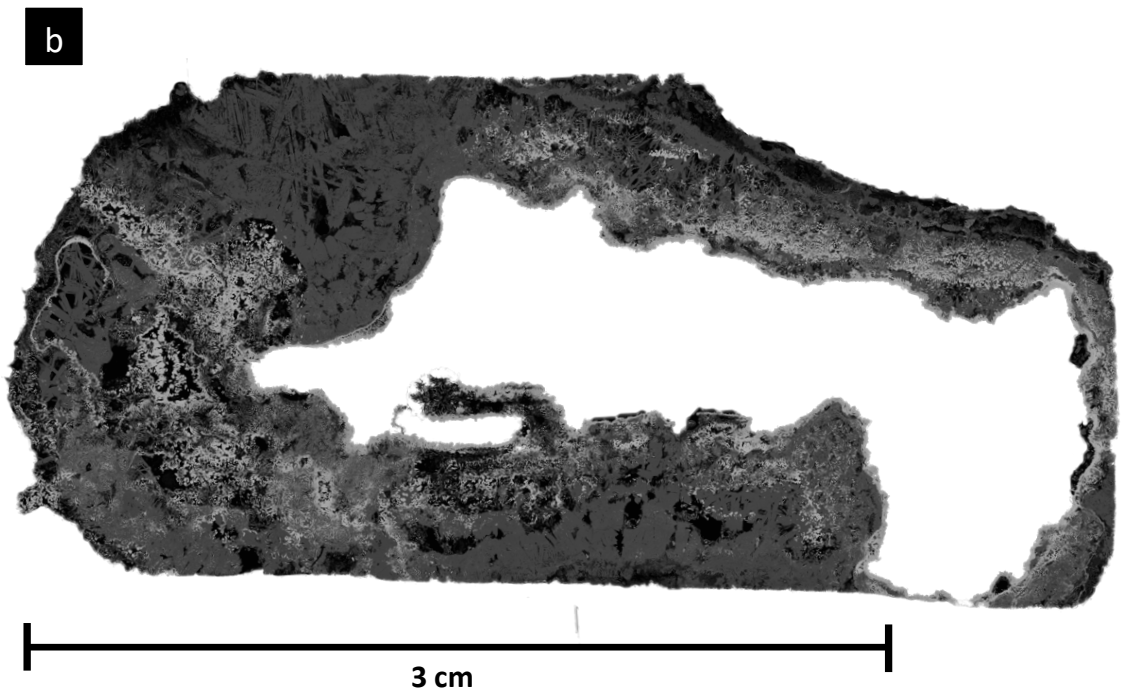
Figure 5.15: *(a) Fåvne third piece printer scan. (b) Fåvne third piece high resolution back scattered map. The scale is approximate.*
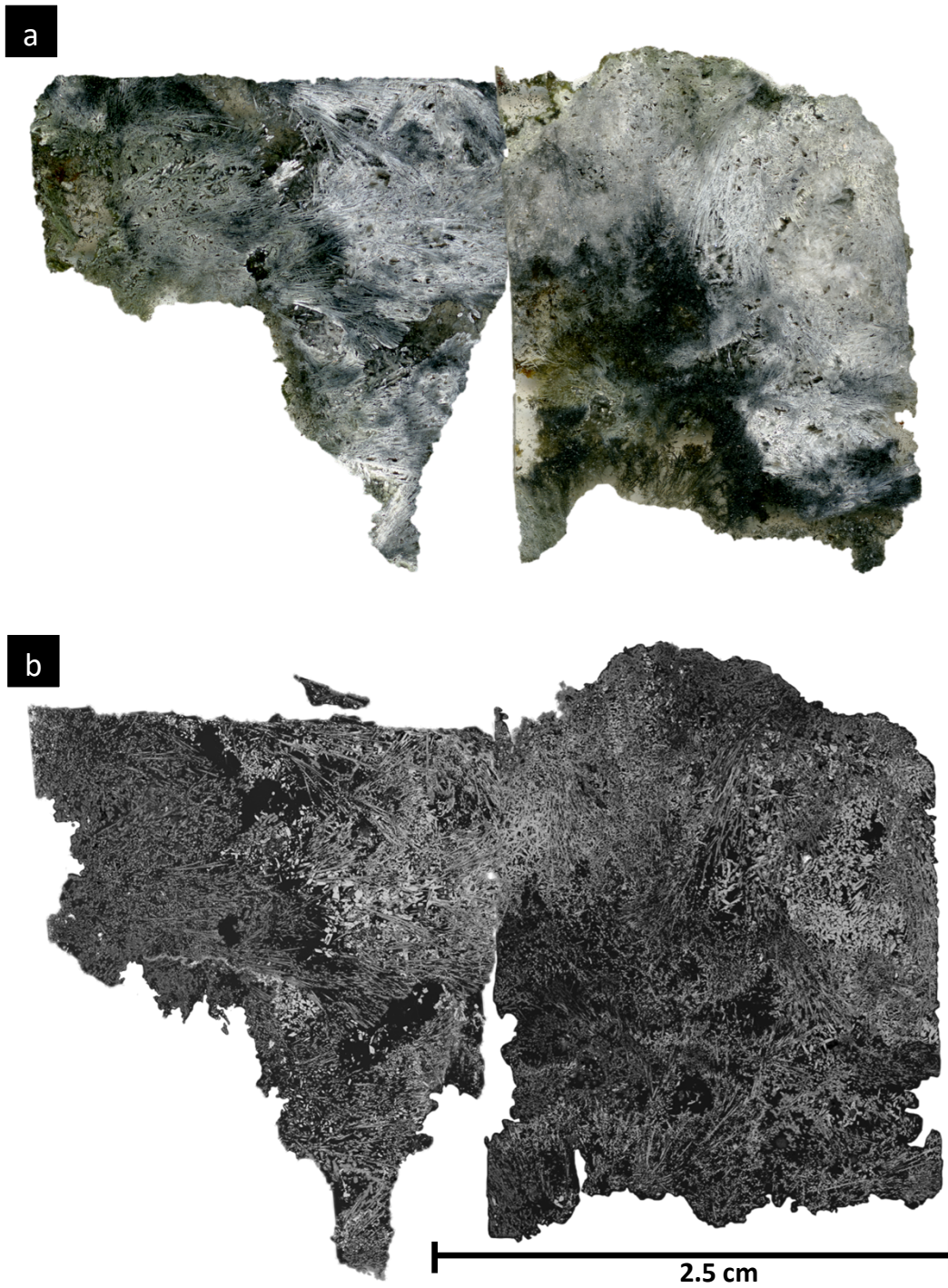
Figure 5.16: *(a) Printer scan of Menorah edge. (b) High resolution back scattered map of Menorah edge. Scale is approximate.*
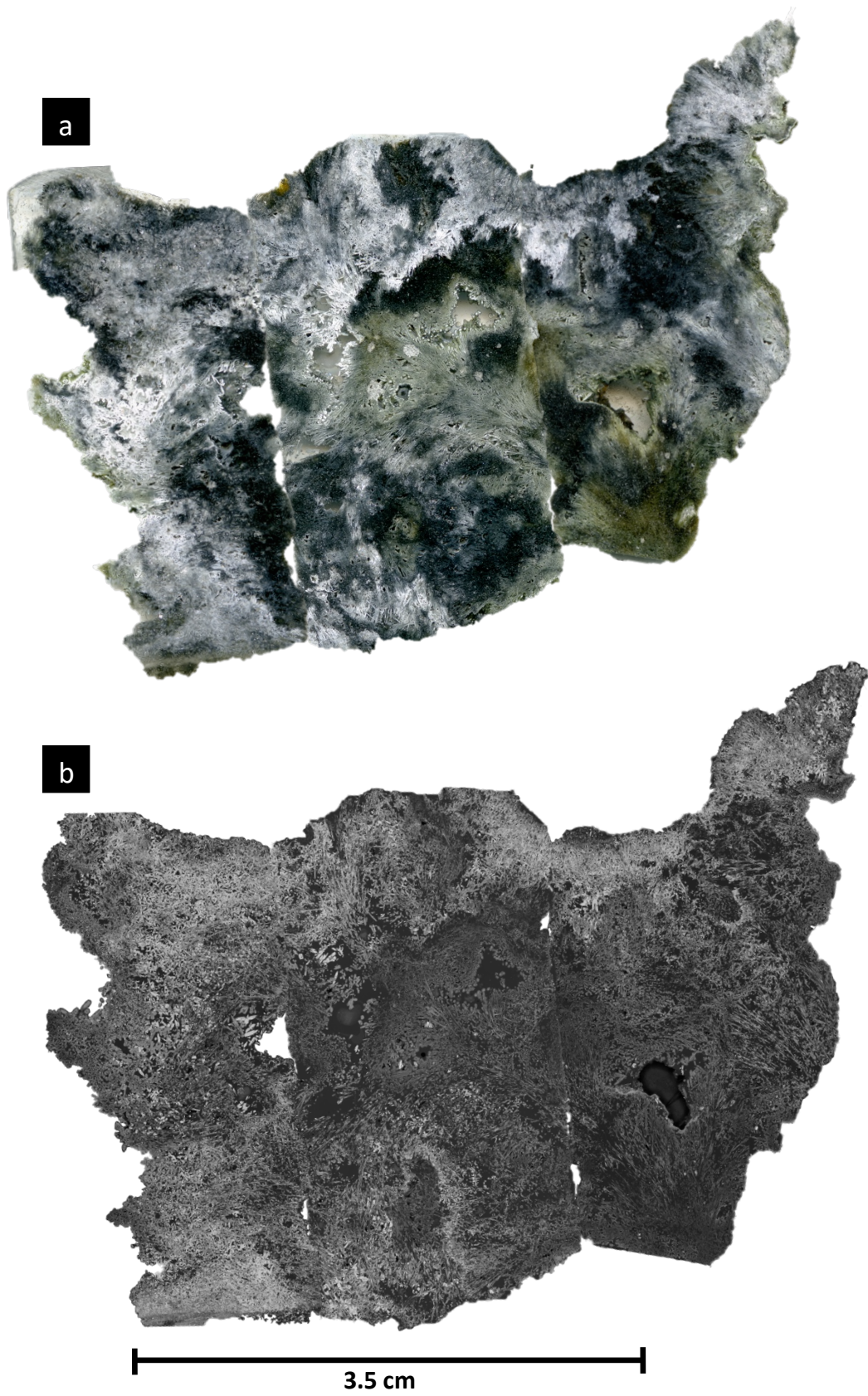
Figure 5.17: *(a) Printer scan of Menorah middle piece and (b) high resolution back scattered maps of Menorah middle piece. Scale is approximate.*

a

b

2 cm
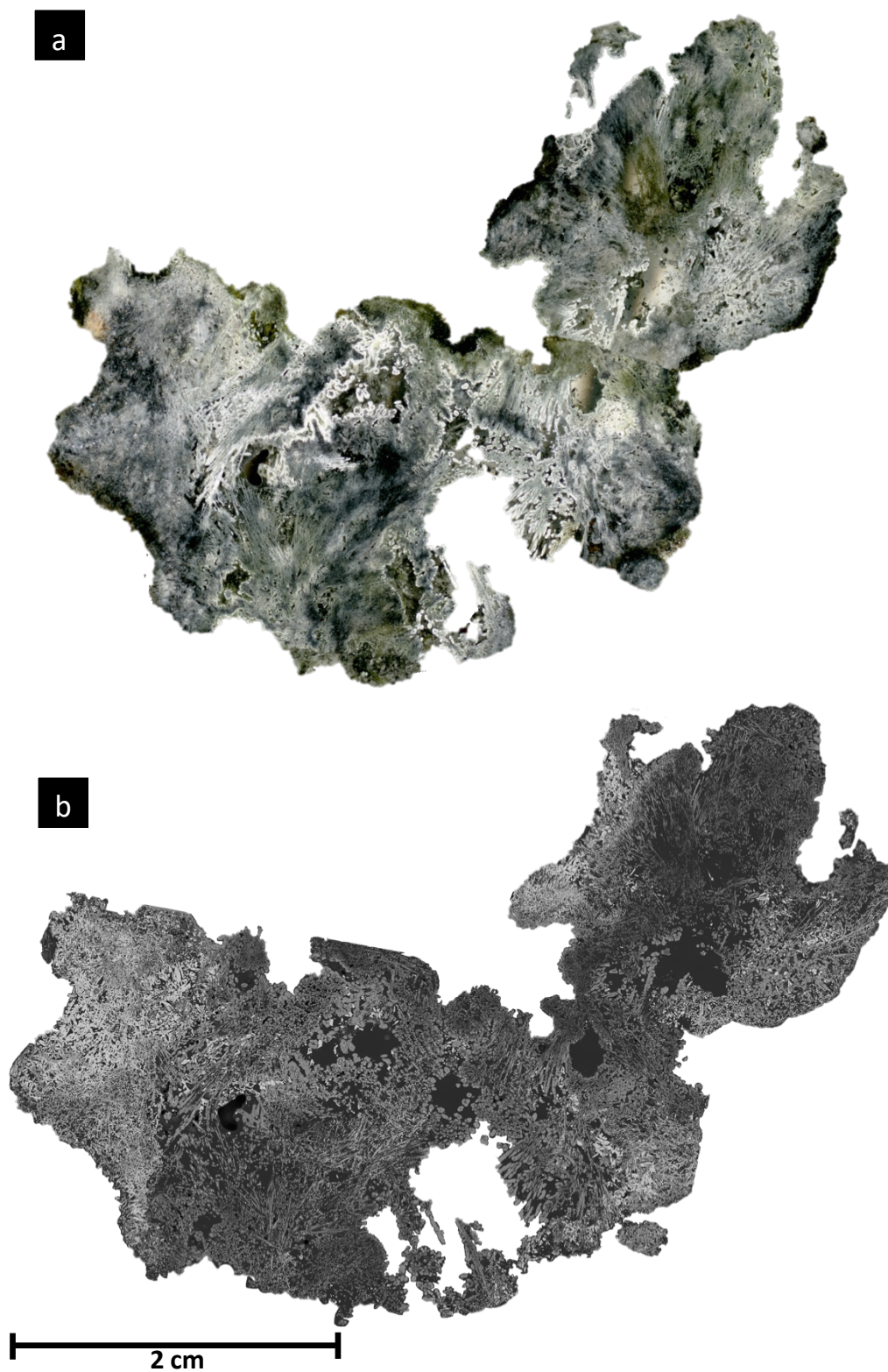
Figure 5.18: (a) *Printer scan of Menorah top piece and (b) high resolution backscattered map of Menorah top piece. Scale is approximate.*

5.5 SEM EDS element analysis and Raman spectroscopy

5.5.1 Fåvne

The results from element mapping suggest the following minerals (Table 5.3). Elemental compositions were suggested by SEM EDS element mapping, whereas the specific minerals were determined based on Raman spectroscopy afterwards.

In the Fåvne North Tower chimney there were two sphalerites with different chemical composition, anhydrite, an iron oxyhydroxide, magnesite and an unknown mineral. Regarding the iron oxyhydroxide, the chemical analysis from SEM and Raman suggest that the mineral is either magnetite or hematite. The Raman spectrometer suggest magnetite. An overview of the results from EDS (supplied with Raman spectroscopy) is presented in Table 5.3 for Fåvne. The minerals are sorted based on the grayscale values produced at the SEM, from heavy to light materials. The elements suggested by the EDS element mapping are given in the column "elements" for each table, whereas further studying at the Raman Spectrometer has revealed the mineral present.

Table 5.3: The table shows the minerals identified after combining SEM element mapping with Raman spectroscopy. Two different sphalerites are identified, suggesting that they have different densities, and therefore also different chemical compositions. There are still two unidentified minerals, one containing Fe and O, which could be an iron oxyhydroxide, and another one containing Fe, Si and O.

Chimney	Minerals	Spesific gravity (g/cm³)	Visual properties SEM (range from light to dark gray)	Elements	Chemical formula
Fåvne	Sphalerite	4.05	1	Zn, S, Fe	$(Zn, Fe)S$
Fåvne	Sphalerite	4.05	2	Zn, S, Fe	$(Zn, Fe)S$
Fåvne	Unknown	-	3	Fe, Si, O	-
Fåvne	Anhydrite	2.97	4	Ca, S, O	$CaSO_4$
Fåvne	Iron oxyhydroxide	-	5	Fe, O	-
Fåvne	Magnesite	3.1	6	Mg, C, O	$MgCO_3$

5.5.2 Menorah

The minerals found in the Menorah chimney were the following: pyrrhotite, barite, sphalerite, anhydrite, and an unknown mineral (Table 5.4). The unknown mineral in the sample contains the elements Mg, Si and O, however there are no clear results as to what mineral it could be

either at the SEM or the Raman spectrometer. The SEM EDS-element mapping provides the elements present in the mineral, but Raman spectroscopy gave inconclusive results when trying to determine what it is. As talc ($Mg_3Si_4O_{10}$) is a mineral that is usually a part of the typical chimney growth (Haymon, 1983), one possible explanation is that the mineral is talc. On the other hand, talc is a sheet silicate and the mineral present in the sample does not bear the same visual similarities as a sheet silicate. The visual attributes of the sample may indicate that the mineral did not have adequate time to grow, and therefore has a subhedral/anhedral crystal shape. The sulfides, pyrrhotite and sphalerite, including barite (sulfate) appear as small crystals most of the time. As pyrite and pyrrhotite have the same element composition, but not same mineral formula, they had to be distinguished at the Raman spectrometer. However, since the crystals were too small, they could not be distinguished using the Raman spectrometer. Given the anhedral/subhedral shape of the identified crystals, it is proposed that the mineral is pyrrhotite, rather than pyrite. Another solution could also be that they are both present in the sample.

Table 5.4: The table gives an overview of the minerals identified with a combination of SEM element mapping and Raman spectroscopy in the Menorah chimney. The minerals are sorted from bright to dark gray.

Chimney	Minerals	Specific gravity (g/cm³)	Visual properties (SEM)	Elements	Chemical formula
Menorah	Pyrrhotite	4.61	Very bright	Fe, S	FeS
Menorah	Barite	4.48	Very bright	Ba, S, O	$BaSO_4$
Menorah	Sphalerite	4.05	Light gray	Zn, Fe, S	(Zn, Fe)S
Menorah	Anhydrite	2.97	Gray	Ca, S, O	$CaSO_4$
Menorah	Unknown antigorite? talc?		Darker than anhydrite	Mg, Si, O	Unknown

5.6 Imaging

As a measure for quantifying the amount of minerals relative to one another, thresholding as an imaging technique was applied to several tiles from the backscattered maps. Based on the pixel size of the picture, and the number of pixels in each color, the measurable amount of each mineral has been quantified. When quantifying the mineral abundances, the picture size was firstly calculated based on the number of pixels in both x and y direction. Thereafter, Image J (fiji) was used to measure the number of pixels for each set of grayscale populations,

that were thresholded based on the grayscale values. These populations have been correlated with the EDS analysis, and thereby connected to the correct mineral. The results of the imaging are shown in the Figures 5.19, 5.20, 5.21, 5.22 and 5.23 below.
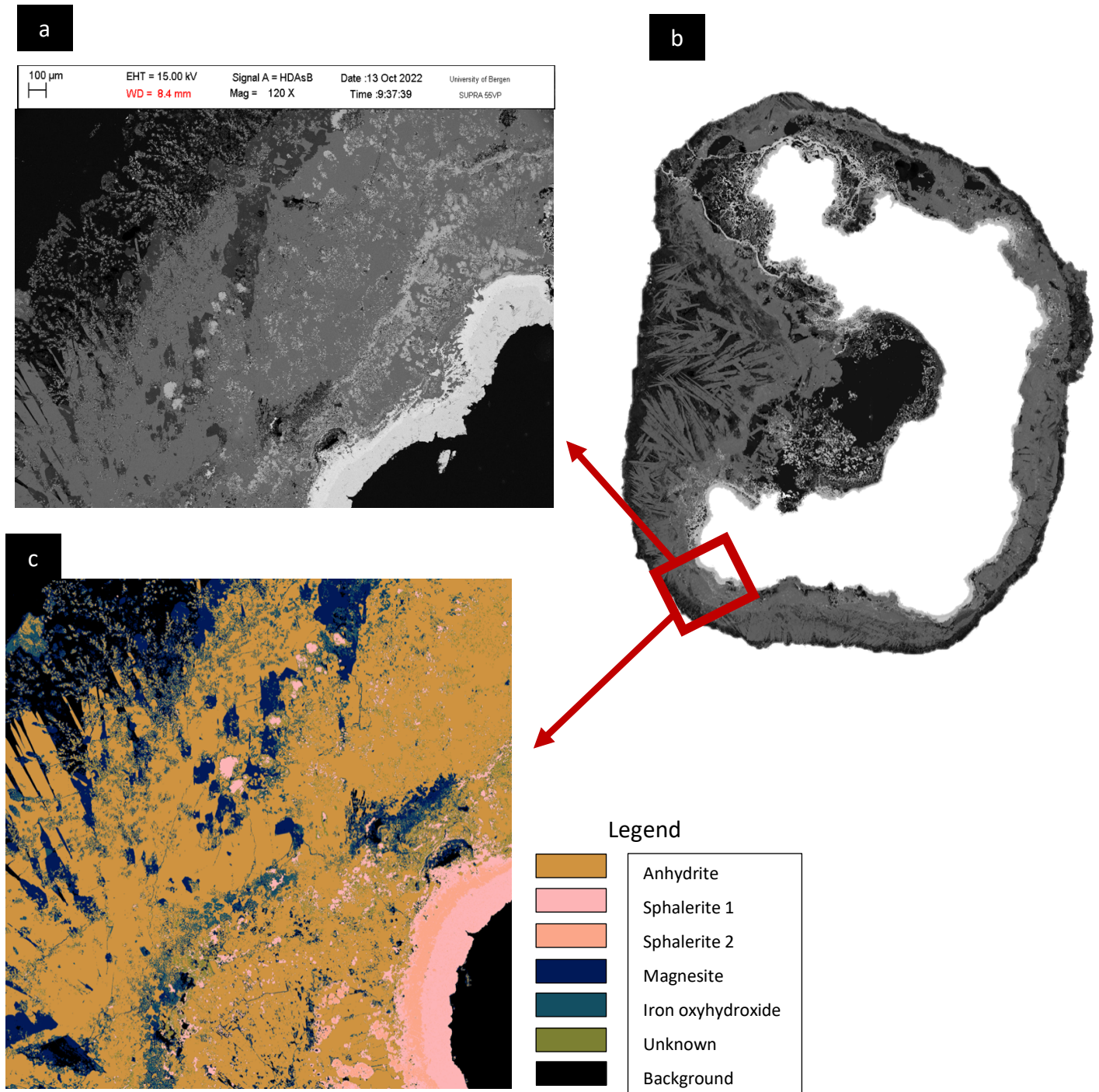
Figure 5.19: (a) Image taken from EDS-analysis at the SEM. (b) High resolution backscattered map, Fåvne First Piece. Scale of the sample is provided in Figure 5.13 (c) Thresholding performed on a tile from the backscattered map, with legend indicating type of material/mineral to the right. Arrows on the illustration represents the area in which the two tiles (a) and (b) are from.

Legend

⬛ (orange)	Anhydrite
⬛ (pink)	Sphalerite 1
⬛ (salmon)	Sphalerite 2
⬛ (dark teal)	Iron oxyhydroxide
⬛ (black)	Background/ anhydrite

Figure 5.20: *(a) Thresholded image of a SEM tile from Fåvne third piece. The legend on the left indicates which material/mineral each color represent, (b) High resolution backscattered image if Fåvne third piece, showing the location and approximate size of the SEM tile that is processed. Scale of the sample is provided in Figure 5.15.*

Legend

▮ (gold)	Anhydrite
▮ (blue)	Mg, Si, O
▮ (pink)	Sulfides/barite
▮ (dark grey)	Bubbles
▮ (black)	Background

Figure 5.21: *(a) Thresholded image of a SEM tile from Menorah middle 3. The legend on the left indicates which material/mineral each color represent, (b) High resolution backscattered image if Fåvne third piece, showing the location and approximate size of the SEM tile that is processed. Scale of the sample is provided in Figure 5.17.*

Legend

🟨	Anhydrite
🟦	Mg, Si, O
🟥	Sulfides/barite
⬛	Background
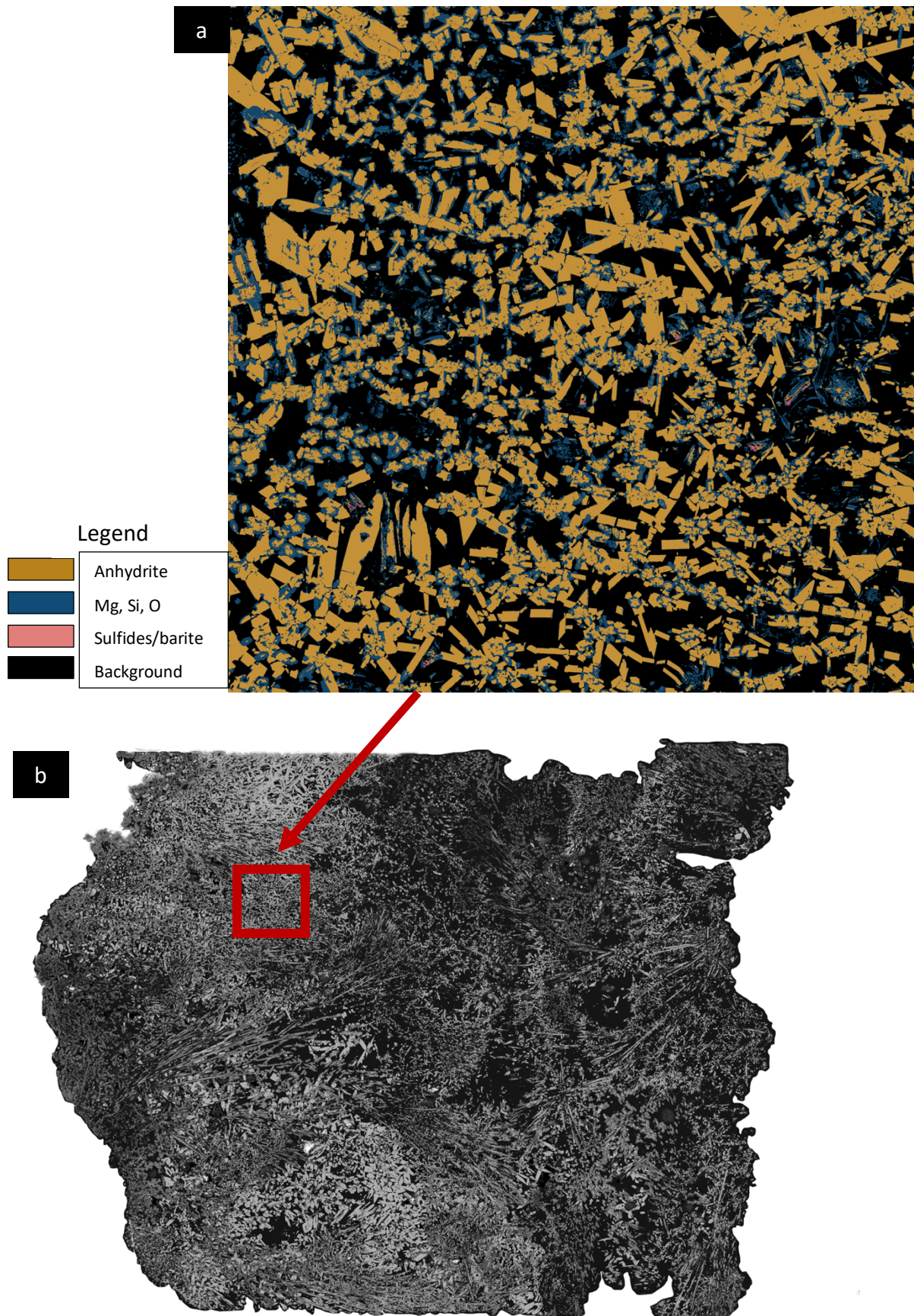
Figure 5.22: (a) Thresholded image of a SEM tile from Menorah edge 1 piece. The legend on the left indicates which material/mineral each color represent, (b) High resolution backscattered image of Fåvne third piece, showing the location and approximate size of the SEM tile that has been processed. Scale of the sample is provided in Figure 5.16.

Legend

🟧	Anhydrite
🟦	Mg, Si, O
🟥	Sulfides/barite
⬛	Background
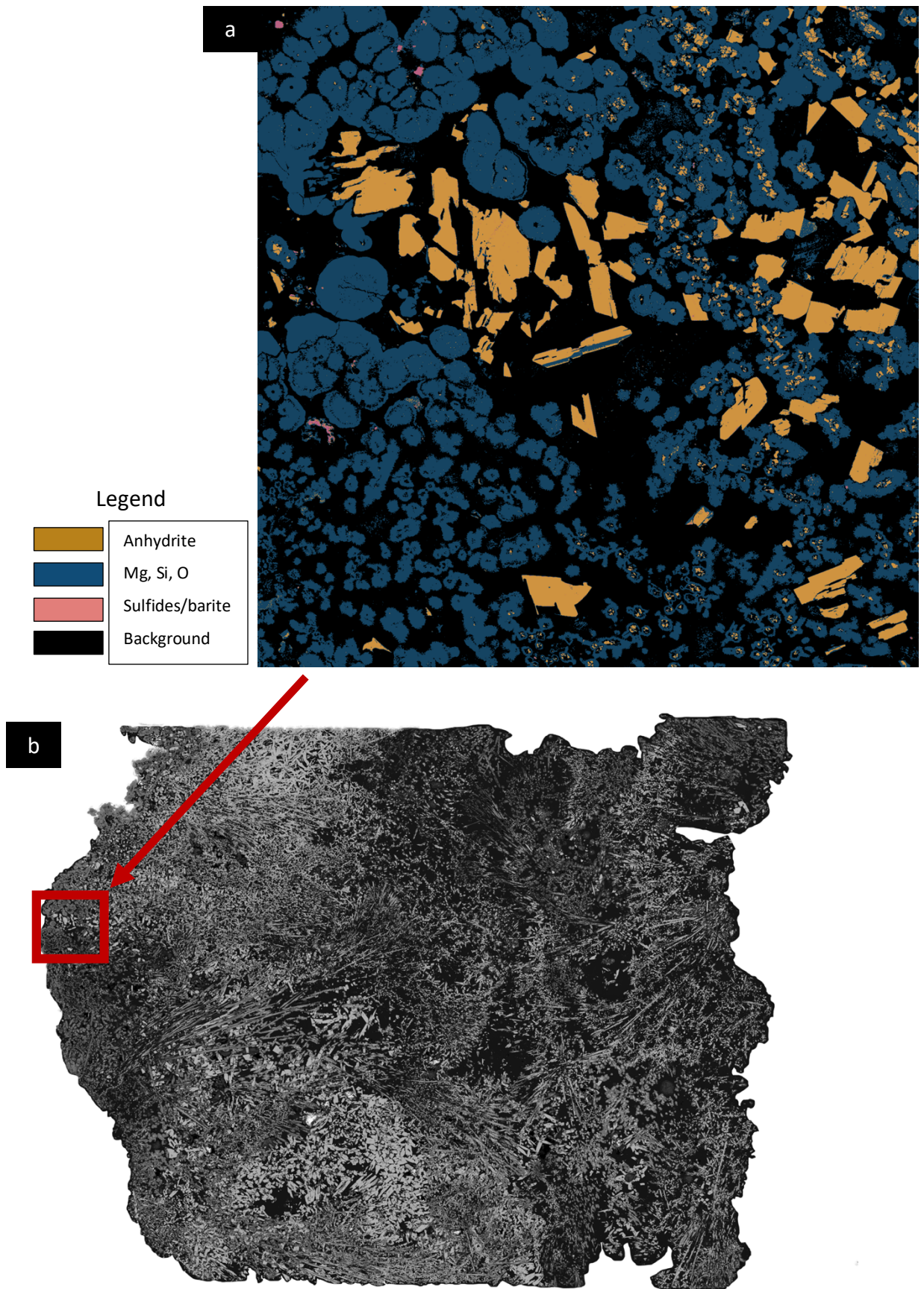
Figure 5.23: (a) Thresholded image of a SEM tile from Menorah edge 1 piece. The legend on the left indicates which material/mineral each color represents, (b) High resolution backscattered image of Fåvne third piece, showing the location and approximate size of the SEM tile that is processed. Scale of the sample is provided in Figure 5.16.

The areas in which calculations were made, were chosen with respect to the rest of the chimney. These areas are therefore believed to somehow represent the mineral ratios that are found throughout the chimneys. Two samples from Fåvne (Table 5.5 and 5.6) and three samples from Menorah (Table 5.7, 5.8 and 5.9) were include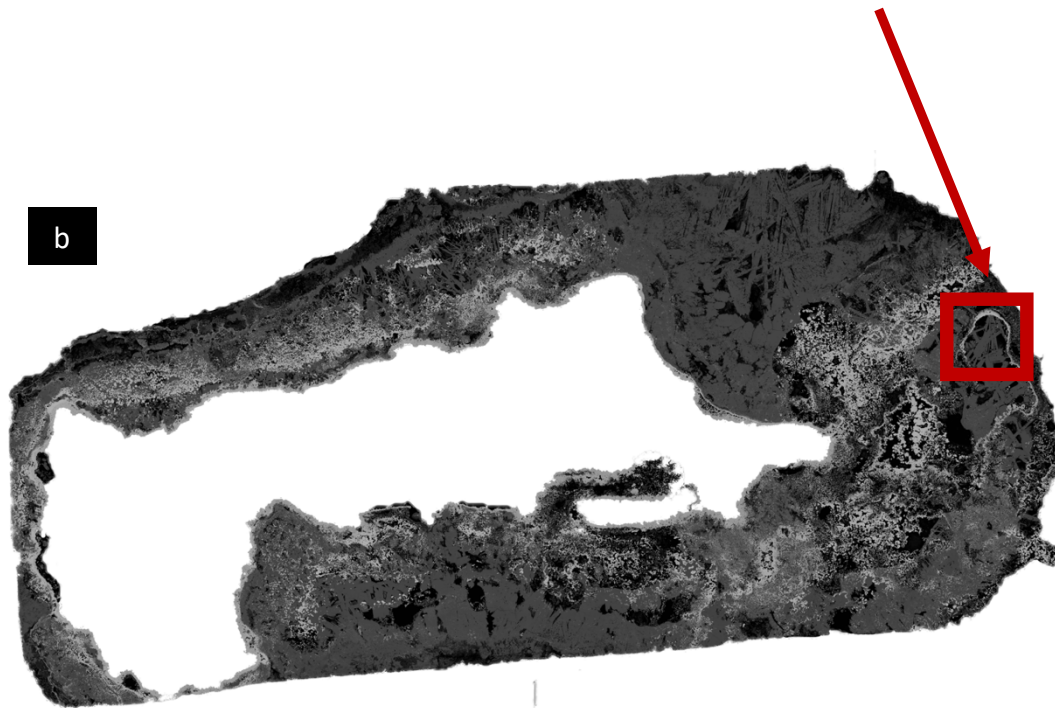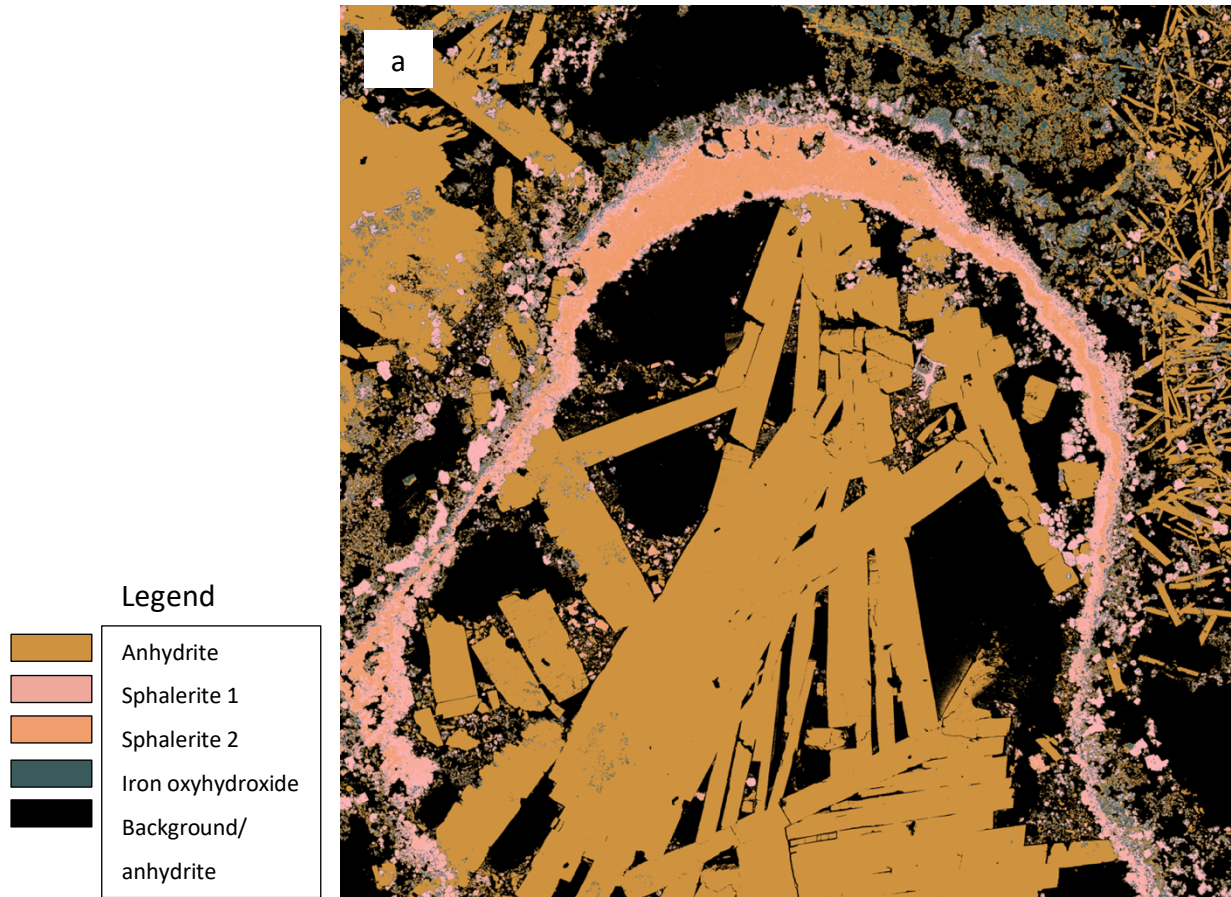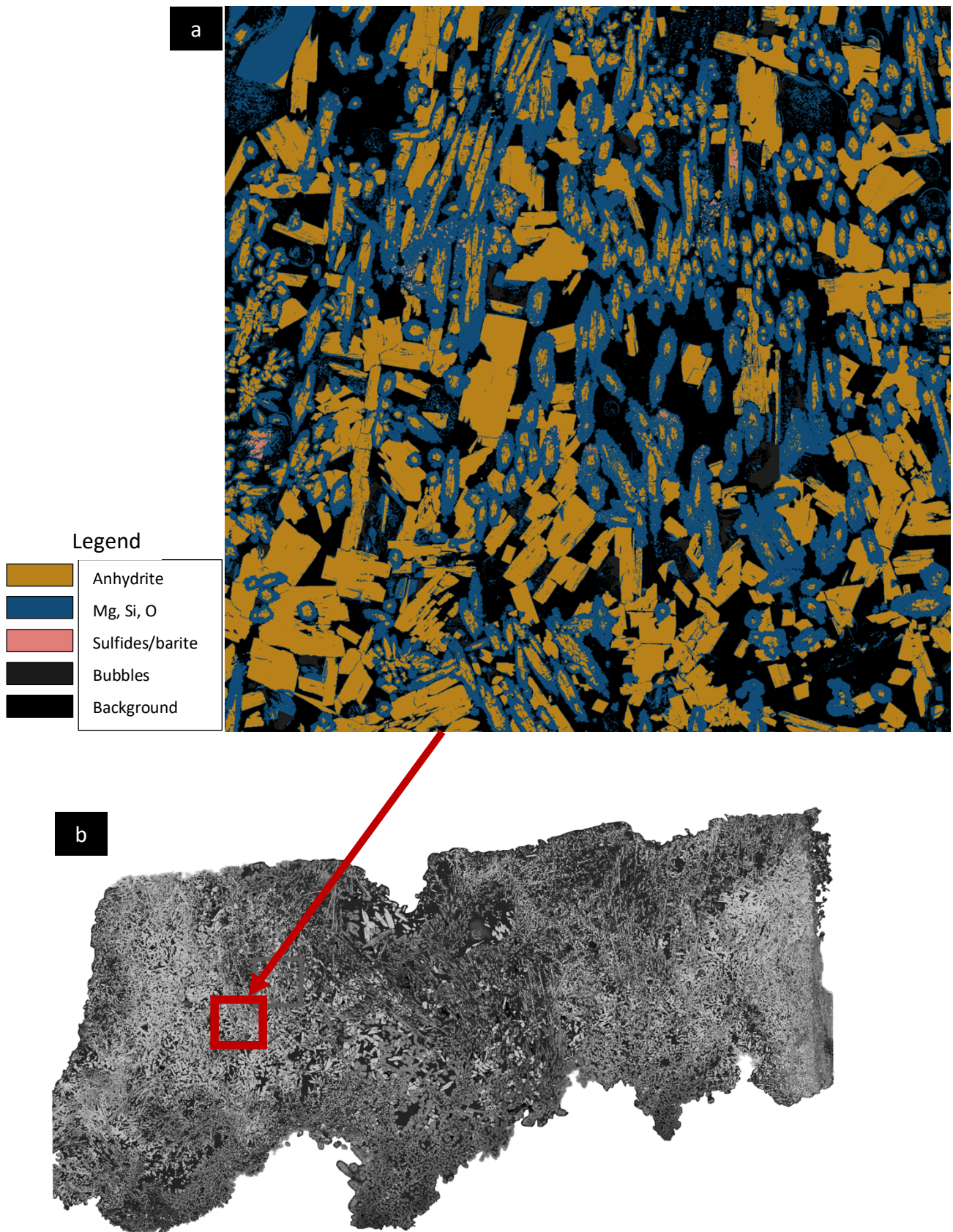d in the calculations. Both calculations from the Fåvne first piece and Fåvne third piece results in anhydrite being the most abundant mineral in the chimney. The most abundant mineral in the Menorah chimney varies depending on the chosen SEM tile.

Table 5.5: Percentages calculated for each mineral in the Fåvne third piece tile from SEM. Correlates with Figure 5.19.

Fåvne first piece tile from SEM		
Size of the picture		
x	1 638	
y	1 638	
total	2 683 044	
	Number of pixels	Percentage
Background:	272 206	10.15
Magnesite:	263 853	9.83
Hematite:	257 660	9.60
Anhydrite:	1 530 622	57.05
Unknown:	111 733	4.16
Sphalerite 1:	193 446	7.21
Sphalerite 2:	53 717	2.00
	Total:	100.01

Table 5.6: Percentages calculated for each mineral in the Fåvne third piece tile from SEM. Correlates with Figure 5.20.

Fåvne third piece tile from SEM		
Size of the picture		
x	4 096	
y	4 096	
total	16 777 216	
	Number of pixels	Percentage
Unknown:	6 365 596	37.94
Anhydrite:	7 597 826	45.29
Sphalerite 1:	1 394 977	8.31
Magnesite/hematite	737 526	4.40
Sphalerite 2:	681 804	4.06
Total:		100.00

Table 5.7: Percentages calculated for each mineral in the Menorah middle 3 piece tile from SEM. Correlates with Figure 5.21.

Menorah middle 3 from SEM		
Size of picture		
x	1 638	
y	1 638	
total	2 683 044	
	Number of pixels	Percentage
Sulfides	7 239	0.27
Anhydrite	883 185	32.92
Background	818 714	30.51
Mg_Si_O	942 407	35.12
Bubbles:	31 572	1.18
	Total:	100.00

Table 5.8: Percentages calculated for each mineral in the Menorah Edge 1 piece from SEM. Correlates with Figure 5.22.

Menorah edge 1 from SEM		
Size of picture		
x	1638	
y	1638	
total	2 683 044	
	Number of pixels	Percentage
Sulfides	7 722	0.29
Anhydrite	1 030 262	38.40
Background	1 192 574	44.45
Mg_Si_O	452 541	16.87
Total		100.00

Table 5.9: Percentages calculated for each mineral in the Menorah edge 1 piece tile from SEM. Correlates with figure 5.23.

Menorah edge 1 from SEM		
Size of picture		
x	1 638	
y	1 638	
total	2 683 044	
	Nr pixels	percentage
Sulphides	7 928	0.30
Anhydrite	271 058	10.10
Background	1 402 495	52.27
Mg_Si_O	1 008 203	37.58
		100.25

After completing the thresholding interpretation in Avizo, the amount of each of the interpreted materials was calculated (Table 5.10 and 5.11). For the Fåvne chimney, there were 72.19% anhydrite, 14.18 % magnesite (etc.) and 13.63 % sphalerite. The Menorah chimney was divided into two materials, whereas there were 52.48% anhydrite and 47.52% of the mineral consistent of Mg, Si and O. There is some uncertainty in the values as a result of the thresholding process.

Table 5.10: Overview of the amount of each mineral, sphalerite, anhydrite, and magnesite in the Fåvne chimney, based on the interpretations done in Avizo (interpretations shown in Figure 5.4).

Mineral	Volume	Count	Volume (%)	Count (%)
Sphalerite	1.26	34464614	13.60	13.63
Anhydrite	6.67	183106045	72.23	72.19
Magnesite	1.31	35938605	14.18	14.18
Total	9.24	253509264	100	100

Table 5.11: Overview of the amount of each mineral, anhydrite and unknown (Mg, Si, O) in the Menorah chimney, based on interpretations done in Avizo (interpretations shown in Figure 5.6).

Mineral	Volume	Count	Volume (%)	Count (%)
Anhydrite	17.61	220334092	52.48	52.48
Mg, Si, O	15.95	199501630	47.52	47.52
Total	33.56	419835722	100	100

6. Discussion

6.1 3-D Visualization of chimney structures

As described in the Chapter 5, the three chimney pieces from the Soria Moria Vent Field, Fåvne North Tower and Menorah were scanned in this study. The sample piece from Soria Moria proved to be the biggest of the three and the first sample to undergo scanning which included an extensively modified setup procedure prior to scanning. Four scans were carried out, where the final proved to yield the most reliable results. The internal structure, including a large conduit and smaller fluid pathway were visible on the scan (Figure 5.1). Varying densities which indicate changes in material, were visible close to the edges in some areas. This can be observed on the right-hand side of the chimney and along the inner rim close to the large conduit (Figure 5.1). Furthermore, there were few to no indications of major density changes apart from previously explained.

The interpreted CT-scan 3D model of the Fåvne chimney resulted in 3 main materials (Figure 5.4). This interpreted model is based on the lower few cm of the chimney. When correlated with the 2-D analysis of mineral content in the chimney, these 3 identified materials from the 3D data are most likely the minerals anhydrite ($CaSO_4^-$), sphalerite ($(Zn, Fe)S$), and magnesite ($MgCO_3$). Based on the 2D analyses of the three thick sections, the spatial distribution correlated well with the overall observed spatial relationships in the 3D model, meaning that the positions of the minerals in 2D and 3D match. Sphalerites dominate the inner part of the chimney, whereas the anhydrite and magnesite respectively are deposited further away from the center. This observed mineral assemblage is closely linked to the two-stage growth model explained by Haymon (1983) (See chapter 2). Firstly, an anhydrite ring is precipitated from the 350°C Ca-rich hot fluids venting at the seafloor (Tivey, 1998). At the outer edge of the chimney, sulfide minerals such as sphalerite, pyrite and pyrrhotite start to precipitate. Furter growth ensures that these sulfides are laminated in the walls of the chimney as anhydrite continues to grow. The second stage of the model is dominated by sulfide precipitation that fills the pores in the anhydrite walls, and in some cases substitute the anhydrite (Haymon, 1983). In the second stage, chalcopyrite is mainly precipitated within the inner walls of the chimney, whereas zinc, copper-iron and iron sulfides are filling pores of the chimney as a result of

seawater mixing (Tivey, 1998). However, the abundance of the varying minerals is highly dependent on the temperature of the fluid (Seyfried, 1987, Butterfield et al., 1994), hence temperature conditions when fluids vent determine the minerals precipitated in the chimney. The solubility of sphalerite decreases in high temperature seawater solutions, and is therefore more likely to be abundant in lower temperature systems (Barrett and Anderson, 1988). Whereas on the other hand, black smokers with high abundances of chalcopyrite (or other Cu-rich minerals) are associated with high temperatures, exceeding 300°C (John et al., 2008). As the temperatures of the Fåvne North tower chimney were 228°C, this is probably the explanation for the high sphalerite content and the absence of chalcopyrite.

The Menorah CT 3D model scan suggested two main materials (Figure 5.6). This interpretation was also, just like for the Fåvne chimney, based on the lower few centimeters of the chimney piece. When correlating observations from the 2D optical, SEM and Raman results, these two identified materials (from 3D interpretations) are most likely anhydrite and an unidentified mineral containing Mg, Si and O, which may resemble an amorphous or a microcrystalline phase (see Chapter 6.3). Two main minerals, respectively anhydrite and unknown mineral (Mg, Si and O) are most abundant in the 2D analyses as well, whereas smaller sized sulfides and barite crystals are observed only in the thick sections and not in the CT-scan.

Conduits and other pores are easy to identify and localize at the 3D scans of both chimneys, whereas quantifying the pores in the chimneys are more challenging. CT-scanning provides an advantage by visualizing the spatial mineral abundances in the entire sample, in a non-destructive way. In this way, the morphology of the samples is well preserved. Both these chimneys could be scanned using the original setup for CT-scanning of sediment cores.

6.2 Method limitations

Despite the exciting possibility of visualizing 3D mineralogical variations, there are several limitations inherent to the CT scanning method or the current setup. The first scans revealed complications in relation to the combination of the size and the mineral content of the sample. Few density differences were observed in the Soria Moria chimney. As the resolution of the Soria Moria chimney scan was ~93 μm, the lack of density contrast could be a result of small

mineral crystals that are not intergrown. If the crystals were smaller than ~93µm, they were not detected, hence the density contrast could not have been obtained. Furthermore, materials with high density can cause inconsistencies that result in severe artifacts on the imagery (Figure 5.1 and 5.2) (Kamel et al., 2003). Artifacts occur because the ratio between X-rays traveling through the air versus the ones traveling through thick and dense materials, are often exceeding the dynamic range of X-ray detectors (Sivers, 1995). The artifacts, in this case, can be observed as lines where different densities appear in areas instead of the original density value, for example in areas around a dense object. These lines are often referred to as streaking artifacts (Man et al., 1998) and are observed in all the scanned objects of this study. The most prominent streaking is in the Soria Moria scan (Figure 5.1). Another example is the interpretation of the Fåvne chimney (5.4 a & b). Both the Figure 5.4a and b show evidence of the magnesite (brown material Figure 5.4) on the inside of the chimney as well as the outer rim. However, magnesite is only identified toward the outer rim of the sample by 2D analysis. This implies that the brown area inside the chimney has obtained this grayscale value falsely because of the streaking artifacts.

There are two different factors resulting in the observed streaking in the 3-D scans: 1) beam hardening and 2) scattering. Both can produce dark streaks between two high density materials that are surrounded by bright streaks (Boas and Fleischmann, 2012). Beam hardening is a typical problem for high density materials such as metals and bones and is related to the type of instrument producing the images (Wellington and Vinegar, 1987). A medical CT-scanner uses technology in which X-rays are emitted in a spectrum, rather than as a monochromatic energy, which can result in beam hardening artifacts (Wellington and Vinegar, 1987). Scattering causes photons to be deflected and change direction. Consequently, detected scattered photons leads to more photons being detected in certain areas, resulting in dark streaks in some areas, with bright streaks in between (Boas and Fleischmann, 2012). Increased kV during scans results in harder X-ray beam, which reduce the beam hardening artifacts. Higher kV also gives less tissue contrast, which noticeably reduces the quality of the scans (Boas and Fleischmann, 2012). Meaning that increasing the kV setting on the CT-instrument, the amount of streaking is reduced – although reducing the overall density contrasts in the sample.

The larger Soria Moria chimney piece was challenging to work with, due to the size capacity of the object. Another factor that reduced the quality of the results, was the uneven surface of the chimney, and its associated mineral distribution. The combination of a large uneven chimney piece with high contents of the high-density mineral barite (Table 4.3) resulted in photons being detected multiple times, and therefore creating noise and streaking artifacts (Figure 5.1). The Soria Moria chimney is proven to consist of mainly barite and silica (Pedersen et al., 2010b). In addition to the high being a high density mineral, barite ($BaSO_4$), is a radiopaque mineral because the barium (Ba) in the mineral is a radiopaque metal (Alaçam et al., 1990). A material that is radiopaque/radiodense is opaque to X-rays, and will therefore block the X-rays out rather than letting them pass through (Alaçam et al., 1990). To reduce the streaking artifacts from the barite (and possibly other dense materials), kilovolts and the microampere applied during the scans were increased, which resulted in less streaks but also reduced contrast between the different materials (Figure 5.1). These results all together indicate that samples with high barite content, such as the Soria Moria chimney, or other dense/radiodense minerals may not work well with the CT-scanner.

In an attempt to identify minerals directly from the CT-scan, pure reference minerals of barite, pyrite and anhydrite were mounted on the sample holder with the samples. The goal was to have a reference grayscale value of the 3 minerals, that could be directly linked to the grayscale values obtained from the chimney. However, the scattering and beam hardening described above complicated this, as the greyscales of the reference minerals did not match with the minerals in the chimneys (Figure 5.2). To resolve this issue, 2D analyses such as Raman spectroscopy and SEM analysis were further applied in order to identify the minerals (see Chapter 6.3 for more details).

Another limitation of the CT scanning method is the process of distinguishing between different minerals with similar densities. Several sulfide minerals have relatively similar densities, such as isocubanite ($3.93 \ \mathrm{g/cm^3}$) and sphalerite ($4.05 \ \mathrm{g/cm^3}$), and pyrite ($5.01 \ \mathrm{g/cm^3}$) and marcasite ($4.89 \ \mathrm{g/cm^3}$) (Table 4.3). Looking at the interpretation of the Fåvne chimney (Figure 5.4), 3 minerals were identified based on the grayscale imagery, compared to the 6 minerals observed in the 2D analysis. All the 2D BSE images done at the SEM, distinguishes between the two sphalerite phases by producing different gray scale values for each of them.

However, these differences were not picked up by the CT-scanner. Even though the actual density differences between the two sphalerites are not known, it can be assumed that the density contrasts are not substantial. This indicates that it might be hard to distinguish minerals such as pyrite from marcasite, with applying CT-scanning alone.

6.3 Combining CT-scans with SEM and Raman spectroscopy

To resolve the issue of not being able to determine the minerals present in the chimneys by CT-scanning alone, SEM analysis and Raman spectroscopy was added to the study. Firstly, SEM analyses were applied to the sample pieces from the Fåvne and the Menorah chimney. High resolution backscattered electron (BSE) maps were created, to help navigate the samples easier when doing EDS element mapping. Element mapping on materials of different densities (revealed from the BSE maps) were conducted for all samples. The results include elemental compositions of each mineral, in which a Raman spectrometer was applied for final verification. The Raman revealed that the Fåvne chimney consisted of sphalerite, anhydrite, magnesite, some iron oxyhydroxide and an unknown mineral. Based on image thresholding of the SEM pictures (Figure 5.19 and 5.20), relative abundances were determined as follows: 51% anhydrite, 10.79% sphalerite, 7.12% magnesite, 4.8% of an iron oxyhydroxide, and 2.08% of an unknown mineral based on averaged numbers from image thresholding. On the other hand, the results from the CT-scanner suggested 72.19% anhydrite, 14.18% magnesite, and 13.63% sphalerite as the 3 main identified materials in the chimney (Figure 5.4). Some of the most abundant minerals (anhydrite, sphalerite, and magnetite) in the chimney were also detected in the 3D-data, after correlation of the 3D interpretations, with the 2D analyses. However, the less abundant minerals, were not detected in the CT-scan results. The neglible detection of some mineral might be due to either scanning artifacts or their less abundance within the sample. As the resolution of the Fåvne scan was ~33 μm, all mineral crystals (that were not intergrown with crystals of the same mineral) remained undetected. This can explain why some minerals in the sample is not detected during CT-scans.

Mineral abundances obtained from the CT and SEM can be recalculated to elemental abundances, for comparison with the geochemistry of a previously analyzed bulk rock sample from the Fåvne chimney (Table 6.1). This was done by normalizing mineral abundances to a

total of 100% (to ignore air in the sample), and converting these into elemental abundances in ppm, assuming ideal mineral stoichiometry ($CaSO_4$ for anhydrite, ZnS for sphalerite, etc.). Comparing the results, some elements are much more abundant in the image analysis calculations compared to the measured bulk analysis, and vice versa. Examples of elements more abundant after image processing include Mg, S, and Ca, which reflect the presence of anhydrite and magnesite. On the other hand, some elements are more abundant in the original bulk analysis such as Fe and Zn, which potentially reflect sampling bias towards sulfide-rich minerals upon sample retrieval for bulk analysis. Comparing these datasets with each other, as well as the differences between the CT-data and SEM-data stresses how difficult it is to calculate the abundance of minerals and/or elements in these types of samples.

Table 6.1: The table gives an overview of measured bulk geochemical compositions of the Fåvne chimney and calculated bulk abundances from the image analyses. The bulk geochemistry is measured by ICP-OES in a previous study (Apolline Samin).

Type of measurement/calculation	Mg (ppm)	S (ppm)	Ca (ppm)	Fe (ppm)	Cu (ppm)	Zn (ppm)
Original bulk analysis	10 813	136 936	13 240	152 127	9 812	120 367
Bulk composition (based on SEM)	27 841	210 692	203 799	45 507	0	98 220
Bulk composition (based on CT)	40 866	214 434	212 664	0	0	91 445

Based on SEM and Raman investigation, the Menorah chimney consists of mainly of anhydrite and an unknown (Raman inactive) material containing Mg, Si and O (possibly amorphous or microcrystalline), with traces of barite, pyrrhotite and sphalerite. Based on these findings, the interpretations of the CT-scan done in Avizo could be correlated with actual minerals. Based on the calculated average from image thresholding using the SEM, relative abundances of the substances are: 27.14% anhydrite, 29.9% of the Raman inactive mineral, 0.29 % sulfides and 42.80% background/bubbles. The latter appeared when the sample was mounted in epoxy. The background and bubbles are assumed to be filling the pores of the chimney, and therefore reflect the porosity of the sample. Accordingly, this means that the porosity of the calculated areas is approximately 42.8 % (bubbles and background all together). The Menorah data from the CT-scanner suggests the presence of 52.5% anhydrite and 47.5% Mg, Si, O. As anhydrite and the Mg-, Si- and O- rich mineral were the two most abundant minerals in the chimney, the estimates based on the 3D-thresholding are presumed acceptable. However, these results

do not include the pores in the chimney, due to difficulty distinguishing the pores from the air surrounding the sample. For the Menorah chimney, no sulfide minerals nor barite was identified from the CT data. A reasonable explanation for this could be the small size (Figure 5.11) of the crystals and the relatively low abundance of these minerals within the chimney. The resolution of the Menorah scan was ~33 μm, thus detection of any substances present in smaller grains than 33 remains impossible.

The results from the 3D CT-scans proved to be limited without additional 2D analysis. However, the 3D scans resulted in a good overview of the spatial distribution of the identified minerals in three dimensions. In the Fåvne chimney, sphalerite, anhydrite, and magnesite were identified in the 3D scans. For the Menorah chimney, only anhydrite and the Raman inactive material were identified. Smaller abundances of minerals were not detected, such as the tiny sulfide crystals in the Menorah chimney.

6.4 A new tool for deep sea research?

To enhance future exploration of modern seafloor hydrothermal products such as seafloor massive sulfide deposits, hydrothermal sediment cores, and hydrothermal chimney structures, a CT- scanner could be brought onboard research vessels for more detailed in-situ investigation. As of now, there are two ships, JOIDES Resolution and drilling vessel Chikyu that have brought CT-scanners on board their research cruises for the purpose of scanning cores (Ocean Drilling Program, n. d, Taira et al., 2014). Based on the findings in this study, doing CT-scan analysis of hydrothermal deposits, might not be the most effective analysis to identify the mineralogical composition of samples, as there are several limitations associated with the method. The positive aspect of scanning samples using a CT-scanner is that the method does requires minimum work prior to scanning (unless substantial modifications to the CT-setup need to be applied), as the only step needed to be done is putting the sample safely in the scanner and start the scan. It is a straightforward method in which extensive mineralogical analyses such as optical microscope investigation, Raman spectroscopy, and SEM with EDS analysis is less needed. If future studies include collection of solid cores from SMS deposits, the scanning results might differ from this study. Solid cores taken from SMS deposits, will provide samples with a fixed size and thickness and will therefore eliminate the limitation of

an uneven sample. Since SMS deposits are covering depths from 100s to 1000s of meters below the surface (Boschen et al., 2013), CT-scanning for determining rapid mineral distributions and abundances could be revolutionary. Although, issues related to density hard and the difficulty of detecting smaller mineral abundances would still be relevant if a CT-scanner was brought to the sea as on land.

7. Conclusions

CT-scanning provides an advantage for spatially visualizing the mineral abundance and distribution of minerals in deep sea hydrothermal chimneys. The CT-scan provides spatial visualizations of the identified populations (and therefore minerals) in the chimney, whereas the abundance of the minerals relative to one another could be calculated. This could make estimating resources on the seafloor more feasible. Additionally, the method is easy to perform, as the object just has to be placed in the scanner without needing any form for preparation. Although the method still has limitations:

- Dense minerals are challenging for the X-rays as they produce streaking artifacts to the dataset as a result of beam hardening of scattering. Radiopaque minerals absorb the X-rays, instead of letting them pass through. These appear very bright on the CT-data and may disturb the overall scan.

- The detection of minerals with small grain sizes remains challenging. Some of the minerals in this study, such as small crystals of sulfides and barite in the Menorah chimney, were not detected on the CT-scanned images. These crystals are ~10-30 µm, and most of them are not intergrown with each other (Figure 5.11). As the resolution of both the Fåvne and Menorah chimney pieces scans were ~33 µm, these smaller mineral crystals (that are not intergrown) are below the detection limit of the scan, and therefore not detected.

- Density contrast between minerals with similar densities are difficult to obtain. Anhydrite (2.98 g/cm^3) and magnesite (3-3.1 g/cm^3) however are both identified in the chimney, suggesting that a minimum density difference at a resolution of ~33 µm should be at least 0.02-0.12 g/cm^3.

- The sample size is proven to affect the quality of the CT-scanned images. Size will ultimately affect the photons producing the X-ray imagery. For instance, the Soria Moria chimney piece, which is approximately 60 cm tall, and 25 cm wide proved that size and mineral content produced artifacts to the images. On the other hand, the Fåvne and Menorah chimney pieces are 10-12 cm tall and 2-6 cm wide and were less affected by scanning artifacts.

If the issues related to CT-scanning of hydrothermal chimneys were resolved, this could be a tool for improving the understanding of mineral resources at the seafloor. The spatial distribution gives a possible insight to the quantity of minerals in hydrothermal systems and could make estimations of mineral abundances in for example seafloor massive sulfides (SMS) less complicated. If this same approach were to be applied to cores from SMS deposits, the result might differ. The samples would be more even because they would have been collected as cores. Even samples are easier to scan, as they produce less noise and scanning artifacts during the scans. However, the density issues together with issues related to resolution of the scans will still remain challenging.

8. Recommendations for future research

- Use grayscale image datasets to calculate populations present in the sample. If grayscale data can contribute to distinguishing the mineral populations in the datasets, by applying gaussian mixture modeling or similar methods, then a lot of time can be saved. This could help determine the number of populations in the samples and make the interpretation part of the process less manual.

- To identify all the minerals in this study, additional methods would have to be applied. In this study, one of the main minerals present in the Menorah chimney was an amorphous/not crystalline mineral that remains unidentified. In order to add information to the research in the Loki's Castle area, further analyses have to be applied to identify the unidentified mineral. Suggested methods for identification could be X-ray diffraction (XRD) analysis, Electron Backscattered Diffraction (EBSD) and/or Transmission Electron Microscope (TEM).

- To resolve the problem of scanning large chimneys, scanning the same chimney several times might be a solution. Scanning large samples in a CT-scanner is proven to be challenging. Sivers (1995) suggested that larger objects that needed to be scanned, should be scanned multiple times, where each scan focuses on one part of the chimney. After all parts are scanned, the results could be put together to produce a complete dataset. The signal to noise ratio could also be improved by applying a higher flux to denser regions, making it possible to reduce extreme attenuation differences between air and dense materials (Sivers, 1995).

- Create CT-maps providing the thickness of the chimney walls.

- Calculate/quantify the porosity in hydrothermal chimneys.

9. References

ALAÇAM, T., GÖRGÜL, G. & ÖMÜRLÜ, H. 1990. Evaluation of diagnostic radiopaque contrast materials used with calcium hydroxide. *Journal of Endodontics,* 16**,** 365-368.

ALT, J. 1995. Subseafloor Processes in Mid-Ocean Ridge Hydrothermal Systems. *Washington DC American Geophysical Union Geophysical Monograph Series,* 91**,** 85-114.

BARGE, L. M., JONES, J.-P., PAGANO, J. J., MARTINEZ, E. & BESCUP, J. 2020. Three-Dimensional Analysis of a Simulated Prebiotic Hydrothermal Chimney. *ACS Earth and Space Chemistry,* 4**,** 1663-1669.

BARRETT, T. & ANDERSON, G. 1988. The solubility of sphalerite and galena in 1-5 m NaCl solutions to 300°C. *Geochimica Et Cosmochimica Acta - GEOCHIM COSMOCHIM ACTA,* 52**,** 813-820.

BOAS, F. & FLEISCHMANN, D. 2012. CT artifacts: Causes and reduction techniques. *Imaging in Medicine,* 4.

BOSCHEN, R. E., ROWDEN, A. A., CLARK, M. R. & GARDNER, J. P. A. 2013. Mining of deep-sea seafloor massive sulfides: A review of the deposits, their benthic communities, impacts from mining, regulatory frameworks and management strategies. *Ocean & Coastal Management,* 84**,** 54-67.

BREKKE, H., STENLØKK, J., ERIKSEN, S. H., BJØRNSTAD, A., SANDSTÅ, N. R., SOLVI, K. AND SCHIAGER, P. 2021. *Deep Sea Minerals on the Norwegian Continental Shelf–*

Developments in Exploration [Online]. Available: https://www.npd.no/globalassets/1-npd/fakta/havbunnsmineraler/presentation-deep-sea-minerals-developments-in-exploration-harald-brekke-with-text.pdf [Accessed 10.01.2023].

BUTTERFIELD, D. A., MCDUFF, R. E., FRANKLIN, J. & WHEAT, C. G. 20. GEOCHEMISTRY OF HYDROTHERMAL VENT FLUIDS FROM MIDDLE VALLEY, JUAN DE FUCA RIDGE1. Proceedings of the Ocean Drilling Program, Scientific Results, 1994.

CATHLES, L. M. 2011. What processes at mid-ocean ridges tell us about volcanogenic massive sulfide deposits. *Mineralium Deposita,* 46**,** 639-657.

CEDERSTRØM, J. M., VAN DER BILT, W., STØREN, E. & RUTLEDAL, S. 2021. Semi-Automatic Ice-Rafted Debris Quantification With Computed Tomography. *Paleoceanography and Paleoclimatology,* 36.

CORLISS, J., DYMOND, J. G., GORDON, L., EDMOND, J., HERZEN, R., BALLARD, R., GREEN, K., WILLIAMS, D., BAINBRIDGE, A., CRANE, K. & VAN ANDEL, T. 1979. Submarine Thermal Springs on the Galapagos Rift. *Science (New York, N.Y.),* 203**,** 1073-83.

D. KNIGHT, R., ROBERTS, S. & P. WEBBER, A. 2018. The influence of spreading rate, basement composition, fluid chemistry and chimney morphology on the formation of gold-rich SMS deposits at slow and ultraslow mid-ocean ridges. *Mineralium Deposita,* 53**,** 143-152.

DICK, H. J., LIN, J. & SCHOUTEN, H. 2003. An ultraslow-spreading class of ocean ridge. *Nature,* 426**,** 405-12.

DUBININ, E. P., KOKHAN, A. V. & SUSHCHEVSKAYA, N. M. 2013. Tectonics and magmatism of ultraslow spreading ridges. *Geotectonics,* 47**,** 131-155.

GERMAN, C. & VON DAMM, K. 2006. Hydrothermal processes. *Treatise on geochemistry,* 6**,** 181-222.

GERMAN, C. R., BAKER, E. T., MEVEL, C., TAMAKI, K. & THE, F. S. T. 1998. Hydrothermal activity along the southwest Indian ridge. *Nature,* 395**,** 490-493.

GERMAN, C. R., PARSON, L. M., TEAM, H. S., GERMAN, C. R., PARSON, L. M., BOUGAULT, H., COLLER, D., CRITCHLEY, M., DAPOIGNY, A., DAY, C., EARDLEY, D., FEARN, A., FLEWELLEN, C., KIRK, R., KLINKHAMMER, G., LANDURE, J. Y., LUDFORD, E., MIRANDA, M., NEEDHAM, H. D., PATCHING, J., PEARCE, R., PELLE, H., RADFORD-KNOERY, J., ROUSE, I., SCOTT, J., STOFFREGEN, P., TAYLOR, P., TEARE, D. & WYNAR, J. 1996. Hydrothermal exploration near the Azores Triple Junction: tectonic control of venting at slow-spreading ridges? *Earth and Planetary Science Letters,* 138**,** 93-104.

GERMAN, C. R. & SEYFRIED, W. E. 2014. 8.7 - Hydrothermal Processes. *In:* HOLLAND, H. D. & TUREKIAN, K. K. (eds.) *Treatise on Geochemistry (Second Edition).* Oxford: Elsevier.

HANNINGTON, M., JAMIESON, J., MONECKE, T., PETERSEN, S. & BEAULIEU, S. 2011. The abundance of seafloor massive sulfide deposits. *Geology,* 39**,** 1155-1158.

HANNINGTON, M. D., DE RONDE, C. E. J., PETERSEN, S., HEDENQUIST, J. W., THOMPSON, J. F. H., GOLDFARB, R. J. & RICHARDS, J. P. 2005. Sea-Floor Tectonics and Submarine Hydrothermal Systems. *One Hundredth Anniversary Volume.* Society of Economic Geologists.

HAVFORSKNINGSINSTITUTTET. 2022. *G.O. Sars* [Online]. Available: https://www.hi.no/hi/om-oss/fasiliteter/vare-fartoy/g.o.-sars [Accessed 21.01.2023].

HAYMON, R. M. 1983. Growth history of hydrothermal black smoker chimneys. *Nature,* 301**,** 695-698.

HORIBA SCIENTIFIC. n.d. *What is Raman Spectroscopy?* [Online]. Available: https://www.horiba.com/int/scientific/technologies/raman-imaging-and-spectroscopy/raman-spectroscopy/ [Accessed 20.01.2022 2022].

HOUNSFIELD, G. N. 1972. A method of and apparatus for examination of a body by radiation such as X-or gamma-radiation. *British Patent,* No. 1,283,915.

HSIEH, J. 2003. Computed tomography: principles, design, artifacts, and recent advances. 12-16.

IEA 2021. The Role of Critical Minerals in Clean Energy Transitions. Paris.

JAESCHKE, A., JØRGENSEN, S., BERNASCONI, S., PEDERSEN, R., THORSETH, I. & FRÜH-GREEN, G. 2012. Microbial diversity of Loki's Castle black smokers at the Arctic Mid-Ocean Ridge. *Geobiology,* 10**,** 548-561.

JOHANNESSEN, K. C., VANDER ROOST, J., DAHLE, H., DUNDAS, S. H., PEDERSEN, R. B. & THORSETH, I. H. 2017. Environmental controls on biomineralization and Fe-mound formation in a low-temperature hydrothermal system at the Jan Mayen Vent Fields. *Geochimica et Cosmochimica Acta,* 202**,** 101-123.

JOHN, S., ROUXEL, O., CRADDOCK, P., ENGWALL, A. & BOYLE, E. 2008. Zinc stable isotopes in seafloor hydrothermal vent fluids and chimneys. *Earth and Planetary Science Letters,* 269**,** 17-28.

KAMEL, E. M., BURGER, C., BUCK, A., VON SCHULTHESS, G. K. & GOERRES, G. W. 2003. Impact of metallic dental implants on CT-based attenuation correction in a combined PET/CT scanner. *Eur Radiol,* 13**,** 724-8.

LTD., G. A. P. 2012. Solwara Project, Bismarck Sea, PNG. [no place].

LUSTY, P. A. J. & MURTON, B. J. 2018. Deep-Ocean Mineral Deposits: Metal Resources and Windows into Earth Processes. *Elements,* 14**,** 301-306.

LUYK, E. 2019. *Backscattered Electrons in SEM Imaging* [Online]. Available: https://www.thermofisher.com/blog/materials/backscattered-electrons-in-sem-imaging/ [Accessed 21.01.2023].

MAN, B. D., NUYTS, J., DUPONT, P., MARCHAL, G. & SUETENS, P. Metal streak artifacts in X-ray computed tomography: a simulation study. 1998 IEEE Nuclear Science Symposium Conference Record. 1998 IEEE Nuclear Science Symposium and Medical Imaging Conference (Cat. No.98CH36255), 8-14 Nov. 1998 1998. 1860-1865 vol.3.

MEES, F., SWENNEN, R., GEET, M. V. & JACOBS, P. 2003. Applications of X-ray computed tomography in the geosciences. *Geological Society, London, Special Publications,* 215**,** 1-6.

MURTON, B. J., LEHRMANN, B., DUTRIEUX, A. M., MARTINS, S., DE LA IGLESIA, A. G., STOBBS, I. J., BARRIGA, F. J. A. S., BIALAS, J., DANNOWSKI, A., VARDY, M. E., NORTH, L. J., YEO, I. A. L. M., LUSTY, P. A. J. & PETERSEN, S. 2019. Geological fate of seafloor massive sulphides at the TAG hydrothermal field (Mid-Atlantic Ridge). *Ore Geology Reviews,* 107**,** 903-925.

OCEAN DRILLING PROGRAM. n. d. *Equipment* [Online]. Available: http://www-odp.tamu.edu/publications/210_SR/111/111_3.htm [Accessed 21.01.2023].

PEDERSEN, R., RAPP, H., THORSETH, I., LILLEY, M., BARRIGA, F., BAUMBERGER, T., FLESLAND, K., FONSECA, R., FRÜH-GREEN, G. & JØRGENSEN, S. 2010a. Discovery of a black smoker vent field and vent fauna at the Arctic Mid-Ocean Ridge. *Nature communications,* 1**,** 126.

PEDERSEN, R., THORSETH, I., HELLEVANG, B., SCHULTZ, A., TAYLOR, P., KNUDSEN, H. & STEINSBU, B. 2005. Two Vent Fields Discovered at the Ultraslow Spreading Arctic Ridge System. *AGU Fall Meeting Abstracts,* -1**,** 01.

PEDERSEN, R. B. & BJERKGÅRD, T. 2016. Seafloor massive sulphides in Arctic waters. *Mineral Resources In The Arctic,* 1**,** 209-216.

PEDERSEN, R. B., OLSEN, B. R., BARREYRE, T., BJERGA, A., DENNY, A., EILERTSEN, M. H., FER, I., HAFLIDASON, H., HESTETUN, J. T., JØRGENSEN, S., RIBEIRO, P. A., STEEN, I. H., STUBSEID, H., TANDBERG, A. H. S. & THORSETH, I. 2021. FAGUTREDNING MINERALRESSURSER I NORSKEHAVET LANDSKAPSTREKK, NATURTYPER OG BENTISKE ØKOSYSTEMER. Senter for dyphavsforsking, Universitetet i Bergen.

PEDERSEN, R. B., THORSETH, I. H., NYGÅRD, T. E., LILLEY, M. D. & KELLEY, D. S. 2010b. Hydrothermal Activity at the Arctic Mid-Ocean Ridges. *Diversity Of Hydrothermal Systems On Slow Spreading Ocean Ridges.*

PETERSEN, S., LEHRMANN, B. & MURTON, B. J. 2018. Modern Seafloor Hydrothermal Systems: New Perspectives on Ancient Ore-Forming Processes. *Elements,* 14**,** 307-312.

PETROVIC, A. M., SIEBERT, J. E. & RIEKE, P. E. 1982. Soil Bulk Density Analysis in Three Dimensions by Computed Tomographic Scanning. *Soil Science Society of America Journal,* 46**,** 445-450.

PEYRIN, F., DONG, P., PACUREANU, A. & LANGER, M. 2014. Micro- and Nano-CT for the Study of Bone Ultrastructure. *Current Osteoporosis Reports,* 12**,** 465-474.

RAZI, T., NIKNAMI, M. & ALAVI GHAZANI, F. 2014. Relationship between Hounsfield Unit in CT Scan and Gray Scale in CBCT. *J Dent Res Dent Clin Dent Prospects,* 8**,** 107-10.

RENTER, J. A. M. 1989. Applications of computerized tomography in sedimentology. *Marine Geotechnology,* 8**,** 201-211.

SAHLSTRÖM, F., STRMIĆ PALINKAŠ, S., HJORTH DUNDAS, S., SENDULA, E., CHENG, Y., WOLD, M. & PEDERSEN, R. B. 2023. Mineralogical distribution and genetic aspects of cobalt at the active Fåvne and Loki's Castle seafloor massive sulfide deposits, Arctic Mid-Ocean Ridges. *Ore Geology Reviews,* 153**,** 105261.

SEYFRIED, W. E. 1987. Experimental and Theoretical Constraints on Hydrothermal Alteration Processes at Mid-Ocean Ridges. *Annual Review of Earth and Planetary Sciences,* 15**,** 317-335.

SIVERS, E. A. 1995. Use of multiple CT scans to accommodate large objects and stretch dynamic range of detectability. *Nuclear Instruments and Methods in Physics Research Section B: Beam Interactions with Materials and Atoms,* 99**,** 761-764.

SOULE, S. A. 2015. Chapter 21 - Mid-Ocean Ridge Volcanism. *In:* SIGURDSSON, H. (ed.) *The Encyclopedia of Volcanoes (Second Edition).* Amsterdam: Academic Press.

STEEN, I. H., DAHLE, H., STOKKE, R., ROALKVAM, I., DAAE, F.-L., RAPP, H. T., PEDERSEN, R. B. & THORSETH, I. H. 2016. Novel Barite Chimneys at the Loki's Castle Vent Field Shed Light on Key Factors Shaping Microbial Communities and Functions in Hydrothermal Systems. *Frontiers in Microbiology,* 6.

TAIRA, A., TOCZKO, S., EGUCHI, N., KURAMOTO, S. I., KUBO, Y. & AZUMA, W. 2014. Recent scientific and operational achievements of D/V Chikyu. *Geoscience Letters,* 1**,** 2.

THERMO FISHER SCIENTIFIC 2018. Thermo ScientificTM AvizoTM Software 9 - User's Guide.

TIVEY, M. 1998. The Formation of Mineral Deposits At Mid-Ocean Ridges. *Oceanus,* 41.

TIVEY, M. 2007. Generation of Seafloor Hydrothermal Vent Fluids and Associated Mineral Deposits. *Oceanography,* 20.

VAN DER BILT, W., CEDERSTRØM, J. M., STØREN, E., BERBEN, S. & RUTLEDAL, S. 2021. Rapid Tephra Identification in Geological Archives With Computed Tomography: Experimental Results and Natural Applications. *Frontiers in Earth Science,* 8.

VIEBAHN, P., SOUKUP, O., SAMADI, S., TEUBLER, J., WIESEN, K. & RITTHOFF, M. 2015. Assessing the need for critical minerals to shift the German energy system towards a high proportion of renewables. *Renewable and Sustainable Energy Reviews,* 49**,** 655-671.

VINEGAR, H. J. & WELLINGTON, S. L. 1987. Tomographic imaging of three-phase flow experiments. *Review of Scientific Instruments,* 58**,** 96-107.

WAN, K., CHEN, L. & XU, Q. 2015. Calibration of grayscale values of cement constituents using industrial X-ray tomography. *Science China Technological Sciences,* 58**,** 485-492.

WELLINGTON, S. L. & VINEGAR, H. J. 1987. X-Ray Computerized Tomography. *Journal of Petroleum Technology,* 39**,** 885-898.

WILLEMS, J. S., BANTA, H. D., LUKAS, T. A. & TAYLOR, C. A. 1979. The computed tomography (CT) scanner. *Medical technology: The culprit behind health care costs***,** 116-43.